

NEUROMORPHIC HARDWARE DESIGN

A THESIS

submitted in partial fulfillment of the requirements

for the award of the dual degree of

Bachelor of Science-Master of Science

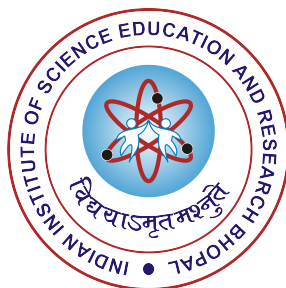
in

**ELECTRICAL ENGINEERING AND COMPUTER
SCIENCE**

by

KHRITISH KUMAR BEHERA

(17125)



**DEPARTMENT OF ELECTRICAL ENGINEERING AND
COMPUTER SCIENCE**
**INDIAN INSTITUTE OF SCIENCE EDUCATION AND
RESEARCH BHOPAL**
BHOPAL - 462066

April 2022



भारतीय विज्ञान शिक्षा एवं अनुसंधान संस्थान भोपाल
Indian Institute of Science Education and Research
Bhopal
(Estb. By MHRD, Govt. of India)

CERTIFICATE

This is to certify that **Khritish Kumar Behera**, BS-MS (Electrical Engineering and Computer Science), has worked on the project entitled '**Neuromorphic hardware design**' under my supervision and guidance. The content of this report is original and has not been submitted elsewhere for the award of any academic or professional degree.

April 2022
IISER Bhopal

Dr. Kuntal Roy

Committee Member	Signature	Date
Dr. Aditya Shankar Medury	_____	02/05/2022
Dr. Mitradip Bhattacharjee	_____	02/05/2022
Dr. Pydi Ganga Mamba Bahubalindrungi	_____	02/05/2022

ACADEMIC INTEGRITY AND COPYRIGHT DISCLAIMER

I hereby declare that this project is my own work and, to the best of my knowledge, it contains no materials previously published or written by another person, or substantial proportions of material which have been accepted for the award of any other degree or diploma at IISER Bhopal or any other educational institution, except where due acknowledgement is made in the document.

I certify that all copyrighted material incorporated into this document is in compliance with the Indian Copyright Act (1957) and that I have received written permission from the copyright owners for my use of their work, which is beyond the scope of the law. I agree to indemnify and save harmless IISER Bhopal from any and all claims that may be asserted or that may arise from any copyright violation.

April 2022
IISER Bhopal

Khritish Kumar Behera

ACKNOWLEDGEMENT

I would like to express my warmest thanks to my advisor Dr. Kuntal Roy for allowing me to work on this project. His advice and guidance carried me through all the stages of this project.

I would also like to thank Mohanlal Naik for taking time out of his busy schedule and providing me with valuable insights. I thank my colleagues Keshav Bihani, Nitanshu Bhagawat Kate, and Lakhvir Singh for their vital aid and discussions. I want to thank the IISER Bhopal community for providing a lively atmosphere full of enthusiasm for Science.

Finally, I would like to thank my mother, grandfather, and the whole family for the support and moral guidance that kept me motivated to pursue my dreams.

Khrithish Kumar Behera

ABSTRACT

We have gone far faster in terms of computation than our human brain. However, biological systems have distinct capabilities like recognizing faces from the crowd, even when wearing a mask. Biological systems require very little power to operate. The ultimate solution for low-power brain-inspired computing is to replicate the brain's neural architecture on a chip.

This project implements a character recognition system using a back-propagation neural network algorithm, whose neural architecture can be processed onto the hardware. The neuron will be made up of multiferroics exploiting its novel spintronic device concepts. As multiferroics have the in-built functionality of weight, sum, and threshold function, they can be harnessed to mimic the processing of a biological neuron. For magnetic characterization, vibrating sample magnetometer is used. For better magnetic characterization and stabilization of the sample, magnetic thermal annealing was used. LabVIEW automation of different instruments such as signal generator, spectrum analyzer, electromagnet, and lock-in amplifier was developed in view of synchronizing and data acquisition. This LabVIEW automation was used to develop a ferromagnetic resonance system in the lab.

We have designed the architecture of neuromorphic hardware, which mimics the human brain's neural architecture. In 2007, Albert Fert and Peter Grünberg were jointly awarded the Nobel Prize in Physics for discovering giant magnetoresistance (GMR). The tunneling magnetoresistance uses an insulator instead of a metallic spacer, which boosts the magnetoresistance more than GMR. The input to the neuron will be given at the piezoelectric layer of the multiferroic composite, and the output from the neuron will come from the tunneling magnetoresistance. Finally, all the neurons will be connected such that the output of one neuron is connected as the input to another neuron.

LIST OF SYMBOLS OR ABBREVIATIONS

α	Damping parameter
γ	Gyromagnetic ratio
ω	Angular frequency
Ω	Volume
ϵ	Strain
σ	Stress
LR	Learning rate
M	Magnetization
M_s	Saturation magnetization
λ	Magnetostriction coefficient
H_k	Coercive field
α_{ME}	Magneto-electric coupling
R	Resistance
G	Conductance
Z	Characteristic impedance
T	Transmission coefficient
Y	Young's modulus
d_{pieze}	Dielectric coefficient of piezoelectric
t_{pieze}	thickness of piezoelectric layer

LIST OF FIGURES

1.1	An ANN with one neuron in input layer, two neurons in the hidden layer, and two neurons in the output layer.	3
1.2	A simple neural network to depict forward propagation.	5
1.3	Step size is larger when far away from minima and small step size when close to the minima.	6
1.4	A simple neural network to depict backpropagation.	7
1.5	Optimizing the neural architecture using testing and training error.	10
1.6	An elliptical cylinder with thickness in x-direction, major-axis in z-direction, and minor axis in y-direction.	13
1.7	Magnetic anisotropy for different value of θ when magnetic field is applied along in-plane hard axis.	13
1.8	Magnetic anisotropy for different value of θ when magnetic field is applied along in-plane easy axis.	15
1.9	Magnetization is perpendicular to the planar surface in PMA. .	16
1.10	Two types of PMA: a. Bulk anisotropy b. Interface anisotropy.	16
1.11	Magnetostriction elongation as a function of applied magnetic field.	18
1.12	Electric, elastic, and magnetic properties of multiferroics. . . .	19
1.13	Giant magnetoresistance with Cr layer sandwiched between Fe layer [3, 4].	20
1.14	Parallel and anti-parallel orientation in a TMR.	21
1.15	Experimental system of magnetic thermal annealing.	23
1.16	The precessing magnetization vector the magnetic sample under the applied magnetic field.	24

1.17	FMR absorption given by the imaginary part of the lorentzian.	26
1.18	Derivative FMR signal plotted against magnetic field [10].	26
1.19	Schematic view of the working principle of atomic force microscopy.	28
1.20	Schematic view of the working principle of vibrating sample magnetometer.	29
1.21	Schematic view of the working principle of X-ray diffraction. .	30
1.22	Reflection and refraction of X-ray beams with change in incident angle θ_i	31
1.23	XRR curve for thickness measurement of MgO/CoFeB sample, measured at UGC-CSR-DAE Indore.	31
1.24	Signal generator: R&S SMB100A	32
1.25	Power Supply: R&S NGL202	32
1.26	Spectrum analyzer: R&S Spectrum rider FPH	33
1.27	Source Measuring Unit (SMU): Keithly 2450	33
1.28	Lock-in amplifier: SRS SR830	34
1.29	Probe station	34
1.30	Oscilloscope: R&S RTM3002	35
1.31	Spin Coater: Holmarc HO-TH-05	36
1.32	Shaker: Remi RS-12R	36
1.33	Hot plate: Neuation iStir HP550	37
1.34	Ultrasonic cleaner: Athena UAC	37
1.35	Hot air oven	38
1.36	Rota Mantle	38
1.37	Nitrogen Gun	39
1.38	Vacuum Desiccator	39
1.39	Muffle furnace: Ridhi RVSW-151	40
1.40	Fume hood	40
2.1	Optimizing first hidden layer	43
2.2	Optimizing second hidden layer	43
2.3	Optimizing third hidden layer	44

2.4	VSM results of before and after MTA of MgO/CoFeB 10nm sample.	45
2.5	LabVIEW automation of power supply R&S NGL202.	46
2.6	VI automation of diode using power supply.	46
2.7	VI automation of resistance using power supply.	47
2.8	VI automation of transistor using power supply.	47
2.9	LabVIEW: Electromagnet automation	48
2.10	LabVIEW: Signal generator automation	48
2.11	LabVIEW: Spectrum analyzer automation	49
2.12	LabVIEW: Lock-in amplifier automation	49
2.13	Experimental system for ferromagnetic resonance.	50
2.14	Schematic of the ferromagnetic resonance system.	50
2.15	Characteristics impedance of coaxial cable.	52
2.16	FMR absorption of a magnetic hard disk sample.	54
2.17	EBL patterns on 3 mm × 1.5 mm Si substrate.	58
2.18	Circular and elliptical EBL patterns.	58
2.19	Sputtering deposition of thin-films.	60
2.20	Hardware architecture of a single neuron.	61
2.21	Neuromorphic hardware architecture of a full neural network.	62

CONTENTS

Certificate	i
Academic Integrity and Copyright Disclaimer	ii
Acknowledgement	iii
Abstract	iv
List of Symbols or Abbreviations	v
List of Figures	vi
1. Introduction	1
1.1 Artifical Neural Networks	2
1.1.1 Architecture	3
1.1.2 Activation function	4
1.1.3 Forward propagation	5
1.1.4 Gradient descent	6
1.1.5 Backpropagation	7
1.2 Character recognition system using neural network	9
1.2.1 Neural architecture	10
1.3 Neural network using spintronics	11
1.3.1 Magnetic anisotropy	12
1.3.2 Magnetic field along in-plane: easy and hard axis	13
1.3.3 Perpendicular Magnetic Anisotropy	16
1.3.4 Magnetostriction	18
1.3.5 Multiferroics and Multiferroic Composites	19

Contents x

1.3.6	Giant Magnetoresistance	20
1.3.7	Tunnelling Magnetoresistance	21
1.4	Magnetic Thermal Annealing	23
1.5	Ferro-magnetic Resonance	24
1.6	Electron Beam Lithography	27
1.7	Atomic Force Microscopy	28
1.8	Vibrating Sample Magnetometer	29
1.9	X-ray Diffraction	30
1.10	X-ray Reflectivity	30
1.11	Signal generator: R&S SMB100A	32
1.12	Power supply: R&S NGL202	32
1.13	Spectrum analyzer: R&S Spectrum rider FPH	33
1.14	Source Measuring Unit: Keithly 2450	33
1.15	Lock-in amplifier: SRS SR830	34
1.16	Probe station	34
1.17	Oscilloscope	35
1.18	Other experimental apparatus	36
1.18.1	Spin coater	36
1.18.2	Shaker	36
1.18.3	Hot plate	37
1.18.4	Ultrasonic cleaner	37
1.18.5	Hot air oven	38
1.18.6	Rota mantle	38
1.18.7	Nitrogen gun	39
1.18.8	Vacuum desiccator	39
1.18.9	Muffle furnace	40
1.18.10	Fume hood	40
2.	Results	42
2.1	Character recognition system using neural network	42
2.1.1	Neural architecture modeling	42
2.1.2	Model output	44
2.2	Improvement of magnetization using magnetic thermal annealing	45

2.3	Development of LabView environment for different instruments	46
2.3.1	Power supply	46
2.3.2	Electromagnet	48
2.3.3	Signal generator	48
2.3.4	Spectrum analyzer	49
2.3.5	Lock-in amplifier	49
2.4	Development of ferromagnetic resonance system	50
2.4.1	Characteristic impedance of coaxial cable	51
2.4.2	Measurement of loss in the coaxial cable, connectors and the waveguide	52
2.4.3	FMR result	54
2.4.4	Schottky diode measurement results	54
2.5	Electron beam lithography patterns	58
2.6	Sputtering deposition	59
2.7	Neuromorphic devices using multiferroics	61
2.7.1	Device architecture	61
2.7.2	Multiferroics	62
2.7.3	Read unit using tunnel junctions	63
3.	Discussions and Conclusions	65
3.1	Future plans	66
Bibliography	71

1. INTRODUCTION

Spin-electronics or so-called spintronics, is a rapidly developing nanotechnology. Spintronic devices can be used to store, process, and communicate information. They also possess in-built functionalities for performing specific tasks efficiently. Spintronic devices can be more energy-efficient than the transistor-based devices since there is no charge movement causing Ohmic dissipation.

In 2007, Albert Fert and Peter Grünberg were jointly awarded the Nobel Prize in Physics for discovering giant magnetoresistance (GMR) [3, 4] back in the 1980s, signifying its remarkable transition from fundamental studies to a critical device technology. For the tunneling magnetoresistance (TMR), instead of a metallic spacer as used in GMR, an insulator is used, which boosts the magnetoresistance more than GMR. Here, we will utilize TMR for sensing the magnetization direction.

Brain-inspired neuromorphic computing is intended to mimic our brains' working principles [27, 39]. The biological neural network is a dense network of interconnected neurons which allows them to compute in parallel. An artificial neural network (ANN) models our brains' neural architecture. ANN is composed of neurons, which perform two primary tasks: Summation of the weighted inputs and applying the activation function on the summed input depicting the firing of a neuron. In the training phase, ANN is trained to get the optimizing parameters of weights and bias. We expect the ANN to perform the desired task with unknown inputs in the evaluation phase. The target is to build such neuromorphic chips using the novel spintronic device concepts.

LabVIEW will be used for automation of various instruments for setting up the ferromagnetic resonance setup [1]. It is a graphical programming

environment designed for automation, testing and validation. It will be used as a centralized system for data acquisition and synchronization of different instruments from different vendors.

1.1 Artifical Neural Networks

An artificial neural network (ANN) is a collection of interconnected neurons represented as nodes, similar to the biological neural network [11]. Mimicking its biological counterpart, the artificial neuron accepts input(s) from other connected neurons through an edge. Each edge has a strength associated with it known as *weight*, w . The *weight* and *bias* are the two optimizing parameters of a neural network.

Each neuron processes through a series of sequential steps, which are represented as *Summation step* and *Activation step*. The summation step performs the summation of the weighted input and the bias term. The output from the summation step is fed into the activation step. The output of the activation step is the final output of the neuron.

The working procedure of a neural network is a two-phase process: *training*, and *evaluation*. The neural network (NN) is trained on training data during the training phase. Training data is a tuple (X, T) , where X is the input and T is the desired output or target. The training data is fed into the NN, and the model learns the underlying feature of the data and optimizes its weight and biases to obtain a minimum error. Then comes the evaluation phase, where the trained NN with optimized weight and bias is used to obtain the output for those inputs for which the network was never trained for [11].

1.1.1 Architecture

In an ANN, all the neurons are connected in a specific architecture, the neural architecture. Fig. 1.1 depicts a simple ANN architecture. The architecture can be viewed as three-layered:**Input layer**, **Hidden layers**, and the **Output layer**.

Input Layer: This layer is the input interface between the neural network and the user. The nodes in this layer receive input from the user and send it to its subsequent layers. The nodes in the input layer do not have the bias term. The number of nodes in this layer is dictated by the problem.

Output Layer: This layer is the output interface between the neural network and the user. The nodes in this layer provide the final output to the user. The number of nodes in this layer is dictated by the problem at put.

Hidden Layers: The hidden layer can be more than one layer. This layer resides between the **Input layer** and the **Output layer**. The majority of the computation in an ANN occurs in this layer. Since the users do not interact with this layer, it is termed the hidden layer.

Following are the rules on how a node is connected to another node

- A node in a layer should not be connected to another node of the same layer.
- Any node should not have self-loop.
- A node should be connected to all other nodes in the next layer.
- A node in any layer should not connect to an another node from the previous layer

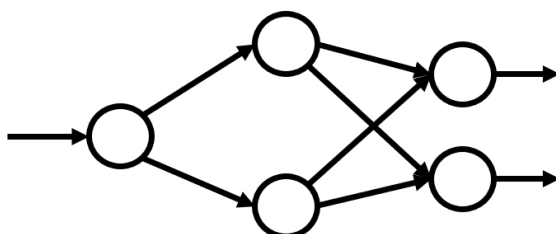


Fig. 1.1: An ANN with one neuron in input layer, two neurons in the hidden layer, and two neurons in the output layer.

1.1.2 Activation function

The activation function is a non-linear mathematical function. It is the only non-linear component in the whole network. The activation function reflects the activation of a biological neuron in a biological neural network. A biological neuron activates or fires only when the input received reaches a certain threshold. This threshold is the biological counterpart of the bias term in an artificial neuron. The most simplistic activation function is a *step* function.

Step function

$$\text{step}(x) = \begin{cases} 1 & \text{if } x > 0 \\ 0 & \text{if } x \leq 0 \end{cases}$$

In general, a smoother version of the step function is used as an activation function known as the *sigmod* function.

Sigmoid function

$$\text{sigmoid}(x) = \frac{1}{1 + e^{-x}}$$

In *deep* neural networks, the number of neurons will be in the millions. Using the sigmoid activation function will be computationally expensive for a larger number of neurons. Hence a computationally inexpensive activation function is deployed known as the Rectilinear Unit function (Relu).

Rectilinear Unit function (ReLU)

$$\text{ReLU}(x) = \begin{cases} x & \text{if } x > 0 \\ 0 & \text{if } x \leq 0 \end{cases}$$

1.1.3 Forward propagation

In forward-propagation, we need to set our neural architecture, after which the input traverses from the input layer to the output layer through the hidden layers. The weight and bias terms have already been configured. In Fig. 1.2 we have taken a very simple ANN with one neuron in the input layer, one in the output layer, and one hidden layer, which consists of one neuron. With weights, W_1 and W_2 , for edges connecting **Node 1** with **Node 2** and **Node 2** with **Node 3** respectively. X is the input given to the NN, and Y is the output received from the NN. **Node 2** and **Node 3** have the bias term B_2 and B_3 respectively. The following figure describes the neural architecture.

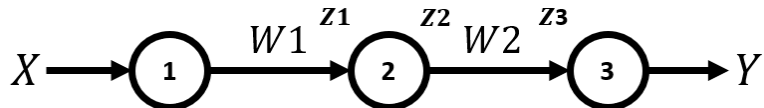


Fig. 1.2: A simple neural network to depict forward propagation.

Generally, the input node does not have any bias term, it's just a simple node, which accepts input and sends it to its subsequent connected node.

Forward propagation steps:

- Input X is provided at the input node, **Node 1**
- Node 1 simply transmits the input to the next node, **Node 2** through the edge with weight W_1
- Input received at node 2 is $Z_1 = X \cdot W_1$
- Node 2 process the input Z_1 and produces the output $Z_2 = \sigma(Z_1 + b_2)$, where b_2 is the bias term of node 2 and σ is the activation function
- Z_2 is transmitted to **Node 3** via the edge with weight W_2
- Input received at Node 3 is Z_3 , $Z_3 = Z_2 \cdot W_2$
- Node 3 process the input Z_3 , and produces the final output of the neural network Y , $Y = \sigma(Z_3 + b_3)$

$$Y = \sigma(Z_3 + b_3) = \sigma(Z_2 \cdot W_2 + b_3) = \sigma(\sigma(Z_1 + b_2) \cdot W_2 + b_3)$$

$$Y = \sigma(\sigma(X \cdot W_1 + b_2) \cdot W_2 + b_3)$$

1.1.4 Gradient descent

Gradient descent is an approach by which the neural network trains itself by minimizing the *error* on changing the weights and biases accordingly.

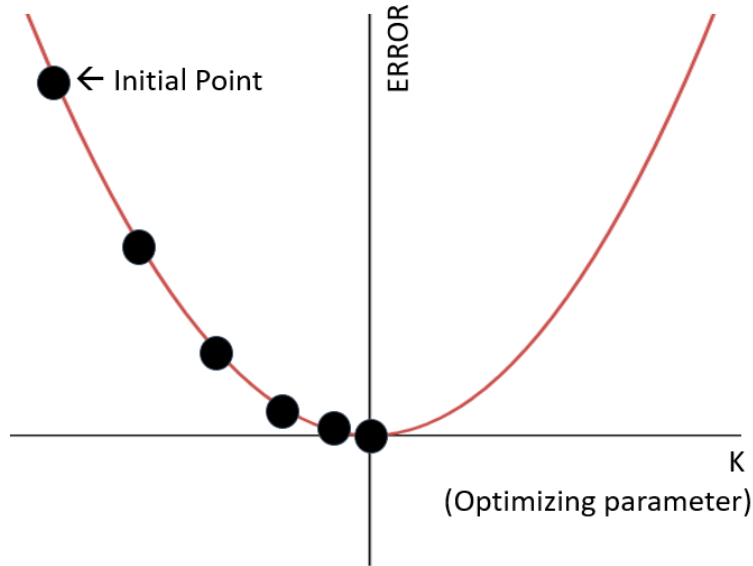


Fig. 1.3: Step size is larger when far away from minima and small step size when close to the minima.

In the Figure 1.3, we have plotted **error** on the y-axis for different values of an **optimizing parameter**, **K**. The optimizing parameter can be any weight or any bias term in the neural network. The aim is to choose a value for K such that the error is minimum.

To begin with, the initial value of K is chosen randomly. The input is traversed through the neural network using the forward propagation method, from which the error is calculated. The slope at that point is computed, suggesting whether to increase or decrease the value of K to minimize the error and the rate at which the minimum error point should be reached. The magnitude of the slope is usually high; hence a *learning rate*, *LR* factor is multiplied by the slope. The LR is usually chosen small but not too small. By multiplying the LR with the slope, the step size is computed, which dictates how much large or small jump K should take. The step size ensures that when K is far away from the minimum, it takes larger step size, and

when K is near to a minimum, it takes smaller step size, in order to avoid overshooting.

$$\text{Step size} = LR \cdot \text{slope}$$

The new value of K is calculated as

$$K_{new} = K - \text{Step size}$$

$$K_{new} = K - LR \cdot \text{slope}$$

$$K_{new} = K - LR \cdot \frac{\partial \text{Error}}{\partial K}$$

The initial value of K is chosen randomly for the gradient descent process; the reason for doing so is if the Error vs. K plot turns out to have a lot of local minima. Moreover, if we always start from a fixed point, there is a heavy chance it will always be at a local minimum. However, if it is chosen randomly, this increases the probability of not getting stuck in local minima. This certainly does not guarantee that it would not be stuck in local minima, but it increases the chance of not getting stuck in one.

1.1.5 Backpropagation

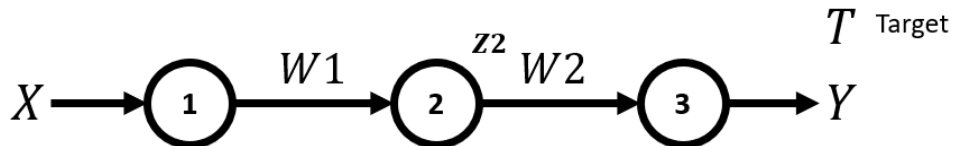


Fig. 1.4: A simple neural network to depict backpropagation.

In forward propagation, it was assumed that all the weights and biases are already optimized. Backpropagation is the process by which the weights and biases are optimized. Backpropagation uses a gradient descent approach on every weight and bias term of the neural network. Since back-propagation is part of the training phase, it is performed on the training data (X, T) , where X is the input and T is the desired output or target. Fig. 1.4 uses the same simplistic neural network chosen in the forward propagation. For input X ,

if Y is the output received for unoptimized weights. Here bias terms are not considered for simplicity. The error is calculated as follows.

$$\text{Error} = (T - Y)^2$$

For optimizing the weight W_1 , gradient-descent approach is used.

$$W_1 = W_1 - LR \cdot \frac{\partial \text{Error}}{\partial W_1}$$

Y is calculated as

$$Y = \sigma(Z_2 \cdot W_2) = \sigma(\sigma(X \cdot W_1) \cdot W_2)$$

From gradient-descent approach,

$$\begin{aligned} \frac{\partial \text{Error}}{\partial W_1} &= \frac{\partial \text{Error}}{\partial Y} \cdot \frac{\partial Y}{\partial W_1} \\ \frac{\partial \text{Error}}{\partial W_1} &= \frac{\partial \text{Error}}{\partial Y} \cdot \left(\frac{\partial Y}{\partial \sigma} \cdot \frac{\partial \sigma}{\partial Z_2} \cdot \frac{\partial Z_2}{\partial W_1} \right) \end{aligned}$$

The new W_1 is computed as

$$W_1 = W_1 - LR \cdot \frac{\partial \text{Error}}{\partial Y} \cdot \left(\frac{\partial Y}{\partial \sigma} \cdot \frac{\partial \sigma}{\partial Z_2} \cdot \frac{\partial Z_2}{\partial W_1} \right)$$

The same process is repeated for all other weights and biases in the neural network, for a number of times, until the minimum possible error is reached.

1.2 Character recognition system using neural network

A character recognition neural network model was implemented in MATLAB. Here the input was a 35-bit word suggesting a noisy alphabet. Moreover, the expected output from the system is a 26-bit word suggesting the original character.

The 35-bit noisy input can be represented in a 7×5 block or pixel, where each pixel can take a value of either 0 or 1. Pixels with value one are represented in black, and those with value zero are represented in white.

For example, the character 'A' can be represented as

A: 01110 10001 10001 11111 10001 10001 10001

If some pixels are altered, it is a noisy character version. The noises can vary from 4-bit flips to 7-bit flips in this model.

The 26-bit output is mapped to the 26 alphabet characters of the English language.

A: 10000000000000 00000000000000

B: 01000000000000 00000000000000

and so on

Z: 00000000000000 00000000000001

The model is trained on the original non-noisy character 35-bit word. After the training, the model should be able to predict the original character even when a noisy character is given as input.

1.2.1 Neural architecture

The neural architecture of the model can be obtained by continually adding hidden layers and hidden neurons and measuring the error, which uses the concept of overfitting and underfitting. If the hidden layer has very few neurons or very few numbers, it will lead to the condition underfitting. In such cases, the input is too complex to be handled by that many few neurons. However, if the number of hidden neurons and hidden layers is very high, the model is overly complex for the given input. The condition is known as overfitting.

In the case of overfitting, the model performs very well on the training data, and the error becomes approximately zero. However, it fails to generalize the input feature, and the error becomes very high for data other than training data (testing data).

In the case of underfitting, the model performs very poorly for both training and testing data. So to find the optimum number of hidden layer neurons and hidden layer, the model should not overfit or underfit. The training error (error while working on the training data) and testing error (error while working on the testing data) are calculated. These errors are plotted against the number of neurons. That neuron is considered where the training and testing errors are close.

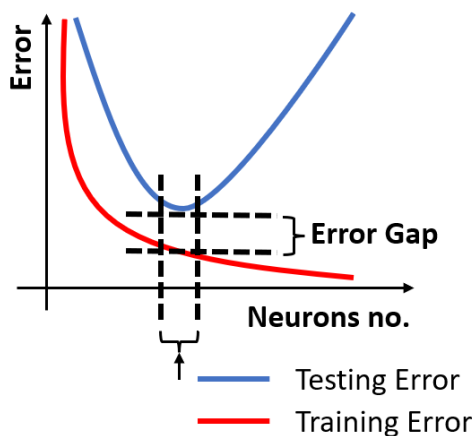


Fig. 1.5: Optimizing the neural architecture using testing and training error.

1.3 Neural network using spintronics

An electron, along with a charge, also contains spin. These spins can be used to store and transmit binary information, the UP spin encoded as 0 and DOWN spin as 1. Spintronic devices are rapidly developing nanotechnologies; they can store, process, and communicate. It is just a matter of spin rotation since there is no charge movement; hence there is no ohmic dissipation, but dissipation due to magnetization damping prevails. In order to change the spin, an external charge voltage/current is applied, which in turn dissipates energy. At 100 nm dimension, all the spins align in one direction, represented as one single large spin. [12, 19]

Multiferroics have gotten much attention in recent days for devising energy-efficient devices [35, 37]. Recently, it has been shown that there can be a high-gain region in the input-output characteristics of the nanomagnets, which can harness the activation function for a neuron [36]. Spintronic devices encapsulate the weight, sum, and activation function, which are the computing elements of the artificial neurons. Spintronic devices are non-volatile, saving us from adding extra circuitry to keep the data intact. Spintronic devices have long endurance, unlike transistor-based devices, which is why such devices are deployed in cars, missions to Mars, etc. It can bear cosmic radiation and other harsh interstellar space environments as well.

1.3.1 Magnetic anisotropy

Magnetic anisotropy refers to different magnetizations in different directions. The magnetization of a specimen depends on its shape. When an external magnetic field magnetizes a specimen of finite size, the free poles which appear on its ends will produce a magnetic field directed opposite to the magnetization. This field is called the demagnetizing field. The intensity of the demagnetizing field H_d is proportional to the magnetic free pole density and, therefore, to the magnetization

$$H_d = N_d \frac{I}{\mu_0}$$

where N_d is the demagnetizing factor, which depends on the specimen's shape.

In the case of a sphere, because of its total symmetry, the demagnetization factor is the same in all directions; hence there is no anisotropy. Anisotropy exists in the case of an ellipsoid, as it is not symmetric in all directions. However, it is difficult to fabricate on a planar wafer because of its oval shape. Which makes an elliptical cylinder the best choice as it has in-plane shape anisotropy, and because of its planar surface, it is easy to fabricate on a planar wafer. The energy is given by

$$E = \frac{1}{2} \Omega M_s H_k \sin^2 \theta$$

Where Ω is the volume of the elliptical cylinder, M_s is the saturation magnetization, and H_k is the coercive field.

1.3.2 Magnetic field along in-plane: easy and hard axis

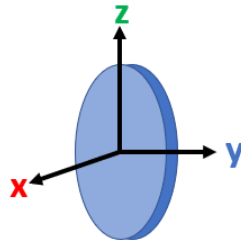


Fig. 1.6: An elliptical cylinder with thickness in x-direction, major-axis in z-direction, and minor axis in y-direction.

Switching magnetization from one direction to the opposite direction by applying a magnetic field in an In-plane easy and hard axis. [5, 25]

In Figure 1.6, we have an elliptical cylinder whose major-axis is in the \hat{z} direction, the minor-axis is in \hat{y} direction, and the thickness is in the \hat{x} direction

For In-plane hard axis

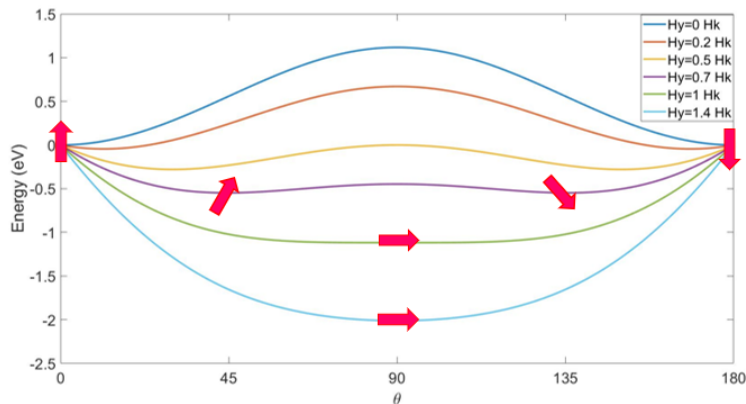


Fig. 1.7: Magnetic anisotropy for different value of θ when magnetic field is applied along in-plane hard axis.

The magnetic field (H_y) is applied along with the \hat{y} direction of the elliptical cylinder. The magnetization vector of the cylinder is making an

angle θ with the z-axis. Let's assume, initially the magnetization vector is along the z-axis (i.z. $\theta = 0^\circ$), on application of magnetic field H_y , can the magnetization vector be made align in (-z)-axis (i.z. $\theta = 180^\circ$)

The anisotropic energy is given by

$$E = \frac{1}{2}\mu_0 M_s H_k \sin^2 \theta - \mu_0 M_s H_y \sin \theta$$

In Fig. 1.2, anisotropic energy is plotted against $\theta(0^\circ - 180^\circ)$ for different values of H_y .

For a given value of H_y , the magnetization vector aligns such that the anisotropic energy is minimum. Hence,

$$\frac{dE}{d\theta} = 0 \implies \theta_{min} = \sin^{-1}(H_y/H_k)$$

The θ_{min} represent the angle made by the magnetization vector with the z-axis such that anisotropic energy is minimum.

When $H_y = 0$, θ_{min} comes out to be 0° , and there is a potential barrier at $\theta = 90^\circ$, which prevents the spontaneous magnetization flipping from $\theta = 0^\circ$ to 180° .

As H_y is increased gradually, the potential barrier at $\theta = 90^\circ$ decreases and the θ_{min} shifts away from $\theta = 0^\circ$, for example, when $H_y = 0.7H_k$, $\theta_{min} = 45^\circ$, i.z. on applying $H_y = 0.7H_k$, the magnetization vector is making an angle of 45° with the z-axis.

When $H_y = H_k$, $\theta_{min} = 90^\circ$ and there is no potential barrier. But on further increasing the H_y to however large value, the θ_{min} does not change, and it still remains at $\theta_{min} = 90^\circ$.

Which suggest that on application of magnetic field along in-plane hard axis will not be able to switch the magnetization to the opposite direction.

For In-plane easy axis

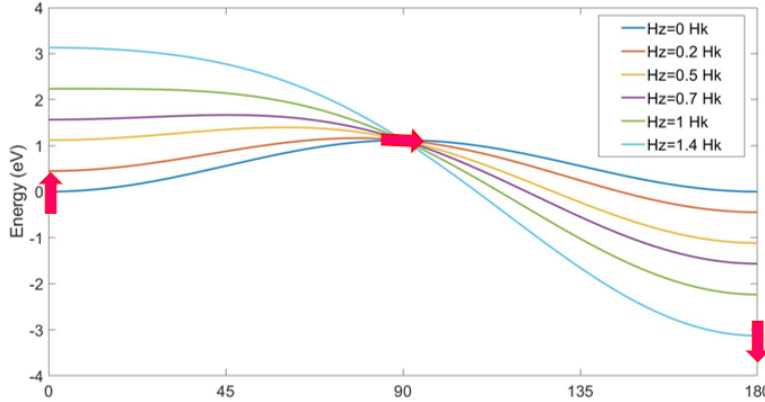


Fig. 1.8: Magnetic anisotropy for different value of θ when magnetic field is applied along in-plane easy axis.

When the magnetic field is applied along the \hat{z} direction of the elliptical cylinder. The anisotropic energy is given by

$$E = \frac{1}{2}\mu_0 M_s H_k \sin^2\theta - \mu_0 M_s H_z \cos\theta$$

For a given value of H_z , the magnetization vector aligns at an angle $\theta_{min} = \sin^{-1}(H_z/H_k)$. In Fig. 1.3, anisotropic energy is plotted against $\theta(0^\circ - 180^\circ)$ for different values of H_z . When $H_z = 0$, θ_{min} comes out to be 0° , and there is a potential barrier at $\theta = 90^\circ$, which prevents the magnetization flipping from $\theta = 0^\circ$ to 180° .

On increasing the H_z , the energy at $\theta = 0^\circ$ side increases and $\theta = 180^\circ$ side decreases, thereby reducing the potential barrier.

When $H_z = H_k$, $\theta_{min} = 90^\circ$ and instead of a potential barrier there is a potential down hill. So on further increasing the θ_{min} becomes 180°

Which concludes that when magnetic field is applied along the in-plane easy axis direction, magnetization switching is possible.

1.3.3 Perpendicular Magnetic Anisotropy

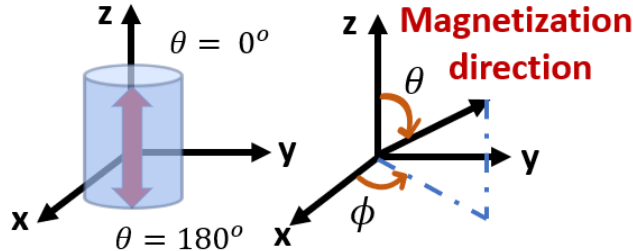


Fig. 1.9: Magnetization is perpendicular to the planar surface in PMA.

If the magnetization is in perpendicular direction to the planar surface, we have perpendicular magnetic anisotropy or PMA. For easy axis, $\theta = 0^\circ$ and 180° and for the hard axis, $\theta = 90^\circ$. The magnet's plane is $\phi = \pm 90^\circ$. Perpendicular magnetic anisotropy is essential as it decreases the lateral dimension, just like transistor scaling, it can accommodate more number of similar magnets in an given finite area [13, 30].

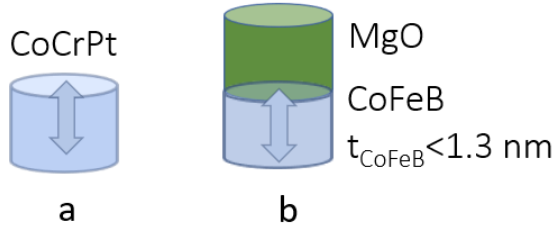


Fig. 1.10: Two types of PMA: a. Bulk anisotropy b. Interface anisotropy.

There are two types of perpendicular anisotropy: a. Bulk anisotropy and b. Interface anisotropy

Bulk anisotropy: In this, the whole material is such that the magnetization is always perpendicular to the planar surface

Interface anisotropy: This anisotropy occurred at the interface of two different materials [13].

The following expression gives the energy.

$$E_{shape}(\theta, \phi) = \frac{1}{2} \mu_0 M_s^2 \Omega N_d(\theta, \phi)$$

Where $N_d(\theta, \phi)$ is the θ, ϕ dependence demagnetization factor, and is given by

$$N_d(\theta, \phi) = N_{d_{xx}} \sin^2 \theta \cos^2 \phi + N_{d_{yy}} \sin^2 \theta \sin^2 \phi + N_{d_{zz}} \cos^2 \theta$$

E_{shape} can be written as

$$E_{shape}(\theta, \phi) = \frac{1}{2} \mu_0 M_s [H_k + H_d \cos^2 \phi] \Omega$$

H_k is the coercive field, H_d is the demagnetization field, M_s is the saturation magnetization, and ω is the volume. For circular cross-section

$$H_d = (N_{d_{xx}} - N_{d_{yy}}) M_s = 0$$

$$H_k = (N_{d_{yy}} - N_{d_{zz}}) M_s$$

Hence, magnetic anisotropy for perpendicular magnetic anisotropy, E_{PMA} can be written as follows

$$E_{PMA} = \frac{1}{2} \mu_0 M_s H_{PMA} \Omega \sin^2 \theta$$

$$H_{PMA} = H_k + H_{interface}$$

1.3.4 Magnetostriiction

Magnetostriiction is a phenomenon where the shape of a ferromagnetic material change during magnetization [7]. The deformation or the strain, $\frac{\partial l}{l}$, generated is usually small and in the range 10^{-5} to 10^{-6} [6]. On increasing the magnitude of magnetic field, the magnetostriiction strain increases. After a certain magnetic field the strain reaches a saturation value λ and known as the magnetostrictive co-efficient [6, 15].

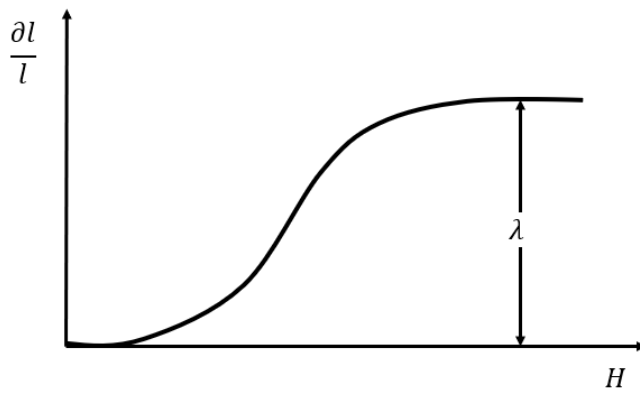


Fig. 1.11: Magnetostriiction elongation as a function of applied magnetic field.

This phenomenon is because the crystal structure inside the domain spontaneously deforms in the direction of magnetization. The strain axis rotates with the magnetization, creating a deformation, generating strain.

The spontaneous strain in the domain is expressed as $e = \frac{3}{2}\lambda$. The magnetostriiction strain depends on the angle ψ , made by the applied magnetic field with the easy axis of the ferromagnetic specimen [6].

$$\Delta\left(\frac{\partial l}{l}\right) = \frac{3}{2}\lambda(1 - \cos^2\psi)$$

The higher the magnetic field, the domain magnetization rotates towards the direction of the applied field. If H is parallel to the easy axis $\Delta\left(\frac{\partial l}{l}\right) = 0$, that is, there will be no elongation or no strain generated.

1.3.5 Multiferroics and Multiferroic Composites

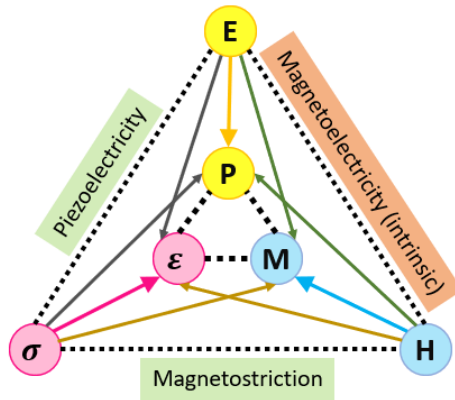


Fig. 1.12: Electric, elastic, and magnetic properties of multiferroics.

In nature, there exist ferroelectric and ferromagnetic materials.

Ferroelectric materials are those materials whose polarization changes on changing the electric field and vice versa. Similar to ferroelectric, the **ferromagnetic materials** are those materials whose magnetization changes on changing the magnetic field and vice versa.

Certain materials possess both the properties of ferroelectric and ferromagnetic materials. These materials are known as **multiferroics**. For a multiferroic material, the polarization changes on changing the magnetic field, and the magnetization changes by changing the electric field.

In the Figure 1.12, the outer node of the triangle, which consists of the electric field **E**, magnetic field **H**, and the stress σ are the physical parameters that can be changed. The inner node of the triangle, which consists of polarization **P**, strain ϵ , and the magnetization **M** are the macroscopic observables of the respective physical parameter.

Ferroelectric material: change in **E** leads to change in **P**

Ferromagnetic material: change in **H** leads to change in **M** and

Ferroelastic material: change in σ leads to change in ϵ

For multiferroic material, there is an intrinsic coupling between **E** and **H**,

known as magneto-electric coupling

$$\alpha_{ME} = \mu_0 \frac{\partial M}{\partial E}$$

At room temperature, the magneto-electric coupling is very weak. So instead of multiferroics, a multiferroic composite is used, a composite of piezoelectric and magnetostrictive materials [24, 38]. Piezoelectric materials are those materials, on applying an electric field, stress is generated at the body and vice versa, and magnetostrictive materials are those materials that generate stress on applying a magnetic field and vice versa. The composition of piezoelectric and magnetostrictive material serves the same purpose of multiferroics with strong magneto-electric coupling. Multiferroic composites are strain-mediated materials [33].

$$\alpha_{ME} = \mu_0 \frac{\partial M}{\partial \sigma} \frac{\partial \sigma}{\partial E}$$

1.3.6 Giant Magnetoresistance

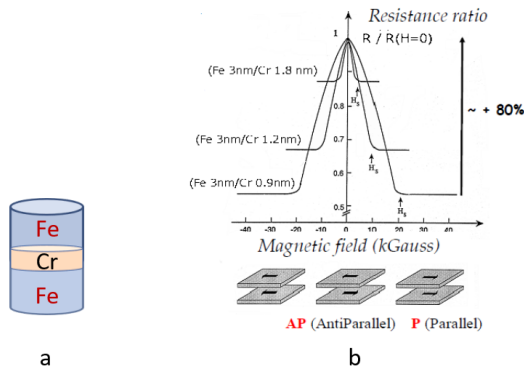


Fig. 1.13: Giant magnetoresistance with Cr layer sandwiched between Fe layer [3, 4].

In 2007, the Nobel prize in physics was awarded jointly to Albert Fert and Peter Grunberg for the discovery of Giant magnetic resistance or GMR. In Fig. 1.13, there is a structure Fe/Cr/Fe; it is seen that on the application of a magnetic field, the resistance along the structure reduces. In Figure

1.13, the resistance ratio vs. Magnetic field is plotted against three different thicknesses of the chromium layer. [3, 4]

The phenomenon's origin is that the magnetization of the Fe layers on either side of the Cr layer is in anti-parallel orientation due to negative exchange interaction through the Cr layer. On application of magnetic field, the spin-dependent magnetic scattering of conduction electron is reduced, which causes a parallel orientation.

The GMR is calculated as follows

$$GMR = \frac{R(0) - R(H)}{R(H)}$$

where $R(0)$ refers to resistance when no magnetic field is applied, $R(H)$ refers to resistance when the magnetic field is applied.

1.3.7 Tunnelling Magnetoresistance

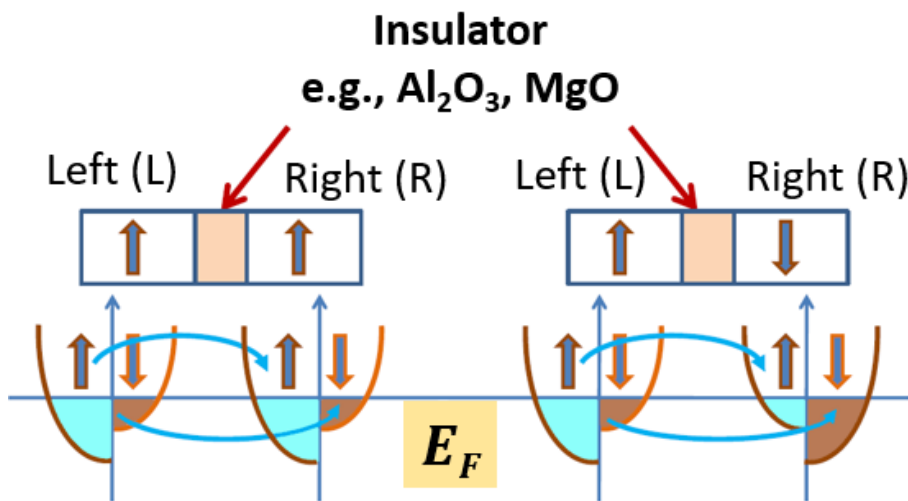


Fig. 1.14: Parallel and anti-parallel orientation in a TMR.

Magnetic tunneling is observed for two ferromagnetic metal layers separated by thin insulating materials like Al_2O_3 , and MgO . Similar to GMR, in the case of tunnelling magnetoresistance or TMR, when the magnetization on both the ferromagnetic layers is in parallel orientation, resistance is low.

When they are in antiparallel orientation, the resistance is high. [14, 21, 40]

This phenomenon occurs because below the Fermi level (E_F), the density of UP states is higher than the density of DOWN states for a UP magnetization. Similarly, for DOWN magnetization, the density of the DOWN state is higher than the density of the UP state.

So for parallel orientation, as shown in Figure 1.14, for both sides of the insulator, below the Fermi level, the density of the UP state is equal on both sides ($N_L^\uparrow = N_R^\uparrow$), similar is the case for DOWN state ($N_L^\downarrow = N_R^\downarrow$). Hence, the states or the electrons can easily tunnel, resulting in low resistance. However, in the case of antiparallel orientation, the respective density of states is not same on both sides. In Figure 1.9, for the antiparallel case, the density of the UP state is high on the left side while the density of the UP state on the left side is low ($N_L^\uparrow > N_R^\uparrow$). Hence the electrons can not efficiently tunnel through the insulator, which results in increased resistance. [9, 20, 26] The conductance is proportional to density of states: $N_L^\uparrow, N_R^\uparrow, N_L^\downarrow, N_R^\downarrow$

$$TMR = \frac{G_P - G_{AP}}{G_{AP}}$$

Where $G_P = G^{\uparrow\uparrow} + G^{\downarrow\downarrow}$ and $G_{AP} = G^{\downarrow\uparrow} + G^{\uparrow\downarrow}$, and the conductance are proportional to the density of states.

$$G^{\uparrow\uparrow} \propto N_L^\uparrow N_R^\uparrow, \quad G^{\downarrow\downarrow} \propto N_L^\downarrow N_R^\downarrow, \quad G^{\downarrow\uparrow} \propto N_L^\downarrow N_R^\uparrow, \quad G^{\uparrow\downarrow} \propto N_L^\uparrow N_R^\downarrow.$$

1.4 Magnetic Thermal Annealing

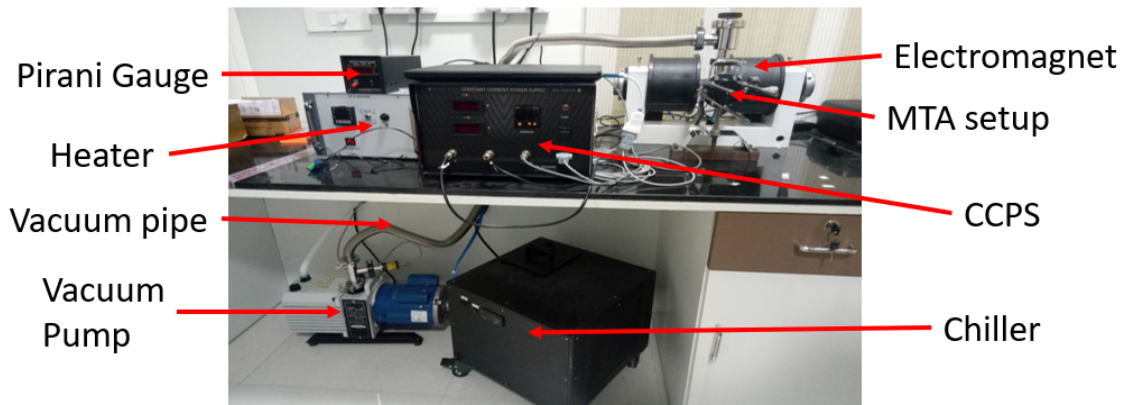


Fig. 1.15: Experimental system of magnetic thermal annealing.

In Figure 1.15, the experimental set-up for magnetic thermal annealing is shown. There is an electromagnet that provides a constant DC magnetic field, which is connected to a Constant Current Power Supply (CCPS) to provide a constant current to the electromagnet; there is a chiller to liquid cool the coils of the electromagnet, then there is the annealing setup, inside which sample is placed. Inside the annealing setup, there is a heater coil, which generates heat. A thermocouple inside the annealing chamber is connected to the heater PID controller which controls the amount and the duration of heating. The magnetic thermal annealing is done in a vacuum, for which there is a rotary vacuum pump connected to the annealing setup. To monitor the vacuum pump pressure, a pirani gauge is connected to the vacuum pump.

1.5 Ferro-magnetic Resonance

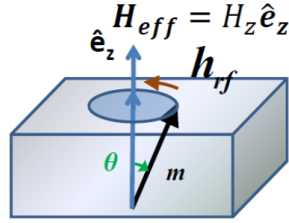


Fig. 1.16: The precessing magnetization vector the magnetic sample under the applied magnetic field.

When a magnetic material is placed in a DC magnetic field, the magnetization vector rotates in a counter-clockwise direction along the direction of the DC field. It is called the precessional motion of the magnetization vector; as it does, it losses energy, and the rotational body falls in the direction of the DC field as shown in Fig. 1.16; this is known as damping [10, 23]. This processing of the magnetization vector is captured by the Landau-Lifshitz Equation [17, 31] (LL Equation):

$$\frac{dM}{dt} = -|\gamma|M \times H_{eff} - \frac{\alpha|\gamma|}{M}M \times M \times H_{eff}$$

where α and γ are the damping parameter and the Gyromagnetic ratio of the magnetic material, respectively. In FMR experiment our aim is to find α of the magnetic material. We will consider α later. The precessional motion of the magnetization vector is given by

$$\frac{dM}{dt} = -|\gamma|M \times H_{eff}$$

DC magnetic field is applied along the z-axis, hence $M_z = M$, and the M_x and M_y has $e^{-i\omega t}$ dependence, hence

$$\frac{dM_x}{dt} = -|\gamma|(H_z + (N_{yy} - N_{zz})M)M_y$$

and

$$\frac{dM_y}{dt} = |\gamma|(H_z + (N_{xx} - N_{zz})M)M_x$$

Solving the above two, we get

$$\omega^2 = |\gamma|^2(H_z + (N_{yy} - N_{zz})M)(H_z + (N_{xx} - N_{zz})M)$$

In case of, sphere: $N_{xx} = N_{yy} = N_{zz}$, therefore, $\omega = |\gamma|H_z$

In-plane FMR: $N_{xx} = N_{zz} = 0, N_{yy} = 1$, therefore, $\omega = |\gamma|\sqrt{H_z(H_z + M)}$

Perpendicular FMR: $N_{xx} = N_{yy} = 0, N_{zz} = 1$, therefore, $\omega = |\gamma|(H_z - M)$

On small rotations [22],

$$\frac{d^2\phi}{dt^2} + \alpha|\gamma|M\frac{d\phi}{dt} + \omega_0^2\phi = 0$$

where $\omega_0 = |\gamma|\sqrt{H_z(H_z + M)}$, for in-plane FMR

To negate the damping, and to keep the magnetization rotating, a transverse AC field $H_y(t) = H_{y0}e^{i\omega t}$ is applied.

$$\frac{d^2\phi}{dt^2} + \alpha|\gamma|M\frac{d\phi}{dt} + \omega_0^2\phi = |\omega|^2MH_{y0}e^{i\omega t}$$

On solving the differential equation, $\phi(t) = \phi_0 e^{i\omega t} = |\phi_0|e^{i(\omega t + \delta)}$, where

$$\phi_0 = \frac{|\gamma|^2 MH_{y0}}{(\omega_0^2 - \omega^2)^2 + (\alpha|\gamma|M\omega)^2}[(\omega_0^2 - \omega^2) - i\alpha|\gamma|M\omega]$$

$$|\phi_0| = \frac{|\gamma|^2 MH_{y0}}{\sqrt{(\omega_0^2 - \omega^2)^2 + (\alpha|\gamma|M\omega)^2}}, \tan\delta = \frac{-\alpha|\gamma|M\omega}{(\omega_0^2 - \omega^2)}$$

The FMR absorption is given by the $\text{Imag}(\phi_0)$, known as the Lorentzian

$$\text{Imag}(\phi_0) = \frac{|\gamma|^2 MH_{y0}\alpha|\gamma|M\omega}{(\omega_0^2 - \omega^2)^2 + (\alpha|\gamma|M\omega)^2}$$

$$\omega = \omega_0, \text{Imag}(\phi_0) = \frac{H_{y0}|\gamma|}{\alpha\omega_0}$$

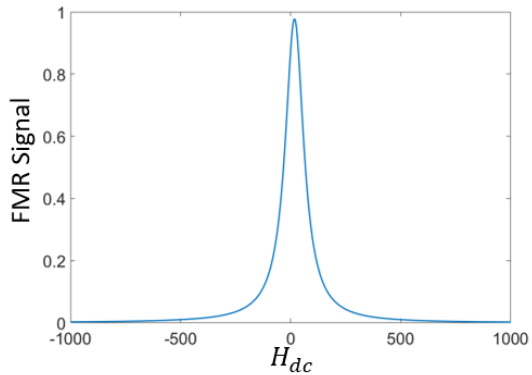


Fig. 1.17: FMR absorption given by the imaginary part of the lorentzian.

The FMR linewidth ΔH , Half width at half maximum (HWHM) is given by:

$$\Delta H = \frac{\alpha\omega_0}{|\gamma|}$$

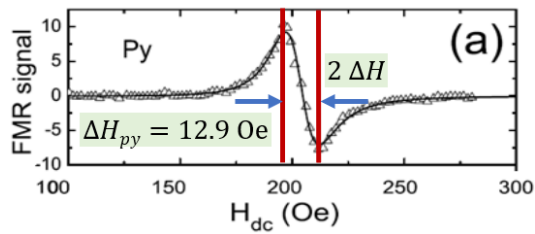


Fig. 1.18: Derivative FMR signal plotted against magnetic field [10].

1.6 Electron Beam Lithography

Electron beam (e-beam) lithography is a method that utilizes an electron gun from a scanning electron microscope. This method is used to draw patterns at nanometer levels. The electrons are exposed to a film of photoresist, which reacts with the electrons. Generally, there are two types of photoresists: positive and negative. When a positive photoresist is exposed to the electron beam, those parts exposed to the electron beam become soluble in the photoresist developer solution. However, when a negative photoresist is exposed to the electron beam, those parts that are exposed become hard, and the rest part becomes soluble in the photoresist developer solution.

- At first, the wafer is cleaned inside ultrasonic cleaner three times with electronic grade acetone and one time with methanol.
- Which then cleaned with DI water to remove any remains of acetone or methanol.
- Then, the wafer is cleaned and dried by blowing a Nitrogen gun.
- After which the wafer is dehydrated to remove moisture using a hot plate.
- Then, the wafer is kept on the chuck of the spin coater, an adequate amount of photoresist is put on the wafer and is rotated at a certain RPM to get the required thickness.
- Once the spin coating is done, the wafer is pre-baked by putting it on a hot plate so that photoresist becomes hard.
- Then electron beam is exposed to the photoresist area.
- Then, the exposed sample is placed inside the developer solution (IPA:MIBK=3:1 + 2% DI water).
- After which sputtering deposition is performed
- Then lift-off process is done by putting the wafer in acetone for 5 minutes at 30°C to remove the photoresist layer.

1.7 Atomic Force Microscopy

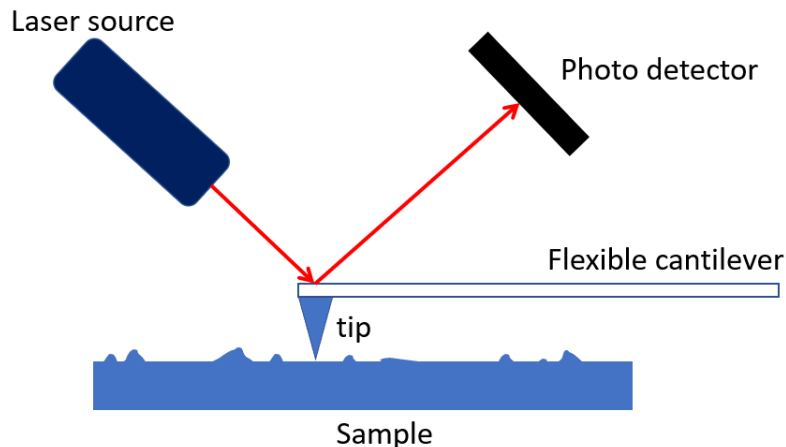


Fig. 1.19: Schematic view of the working principle of atomic force microscopy.

Atomic force microscopy (AFM) is used for imaging the topographical feature of a sample. It consists of a flexible cantilever that holds a tip in the front part of the cantilever. A laser is targeted to the cantilever, which is reflected to the photodetector. The tip scans the sample. It experiences Van der wall's forces, electrostatic forces, magnetic forces, or any other force that arises from the physical interaction between the surface and the tip. This force causes the tip to deflect, and the change in angle of the reflected ray is measured from which the topography of the sample is imaged.

For magnetic material, a magnetic tip is used. Since the tip is magnetized, it is either attracted or repelled from the sample based on the magnetization direction of each domain. Based on the force acting on the tip, the cantilever moves up and down, deflecting the laser received at the photo detector. Based on the degree of deflection, the imaging of the sample is done.

1.8 Vibrating Sample Magnetometer

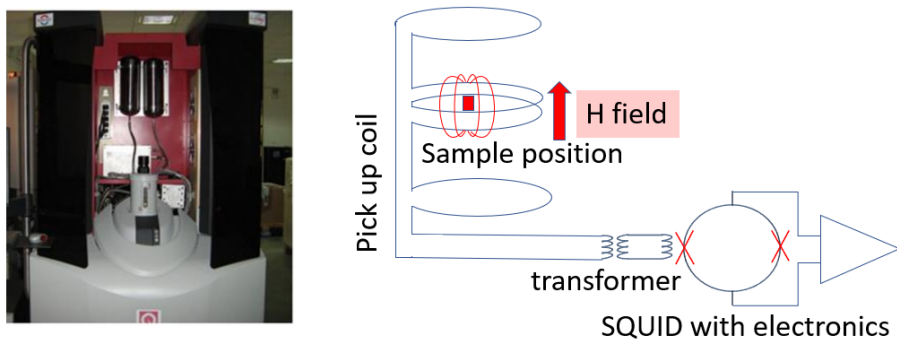


Fig. 1.20: Schematic view of the working principle of vibrating sample magnetometer.

Vibrating sample magnetometer (VSM) is a highly sensitive instrument used for precise magnetic moment measurements. It operates on the basic principle of Faraday's law. It is useful in measuring the magnetic behavior of a magnetic material.

The instrument consists of an electromagnet, which generates a constant DC magnetic field. There is a driver rod over which the magnetic sample is pasted. The rod can oscillate in the vertical direction with some fixed frequency and amplitude. When the sample is brought into the DC field, the constant magnetic field magnetizes the sample, and the magnetization vector aligns in the direction of the DC field. Due to this, the samples create its own magnetic field when the driver rod starts oscillating—the magnetic field due to the sample changes with respect to the time. There are pick-up coils beside the sample, which pick up the alternating magnetic field and generates an electric field in the pick-up coil based on Faraday's law. The induced current is then amplified and sent to the Superconducting Quantum Interference Device (SQUID).

1.9 X-ray Diffraction

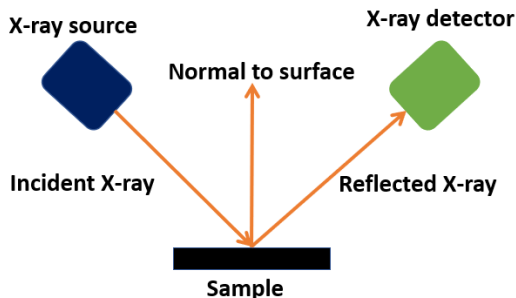


Fig. 1.21: Schematic view of the working principle of X-ray diffraction.

X-ray diffraction (XRD) is a technique used to identify the deposited materials. The XRD system consists of an X-ray tube that emits an X-ray, then there is a sample holder to hold the sample, and there is an X-ray detector. The X-rays are produced in the cathode ray tube; when these X-rays hit the atom of the target material, it knock out the inner shell electrons of the target, thereby imparting energy to the atom. This energy is again released by the atom, which generates characteristics of X-ray spectra. These spectra are filtered to produce monochromatic X-rays; these X-rays are directed onto the sample. The sample and the detector are rotated, and the intensity of the reflected X-ray is recorded. When the incident monochromatic X-rays are directed toward the sample, if it satisfies the Bragg equation, constructive interference occurs, and a peak in intensity is measured.

1.10 X-ray Reflectivity

X-ray reflectivity (XRR), is a measurement technique that uses X-ray reflection intensity to determine the thickness of a multilayer thin-film structure. When an X-ray beam falls on the surface of a layer, if the incident angle, $\theta_i < \theta_c$, where θ_c is the critical angle, total reflection occurs, if $\theta_i = \theta_c$ the beam propagates along with the layer, and if $\theta_i > \theta_c$ some part of the beam reflects and refracts.

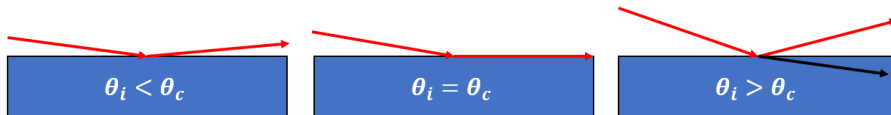


Fig. 1.22: Reflection and refraction of X-ray beams with change in incident angle θ_i .

The X-ray intensity curve is plotted between the intensity of the reflected X-ray and the incident angle. When an X-ray beam falls on the surface of the layers, some part of the beam is reflected, and some part gets refracted. The observed x-ray scattering is the sum of individual electron scattering. When the reflected ray hits another layer, it is either totally reflected or reflected and refracted. This reflected ray from the interface of 1st and 2nd medium interfere with each other, which gives rise to oscillation. This oscillation depends on the film thickness; the thicker the film, the shorter the oscillation time period.

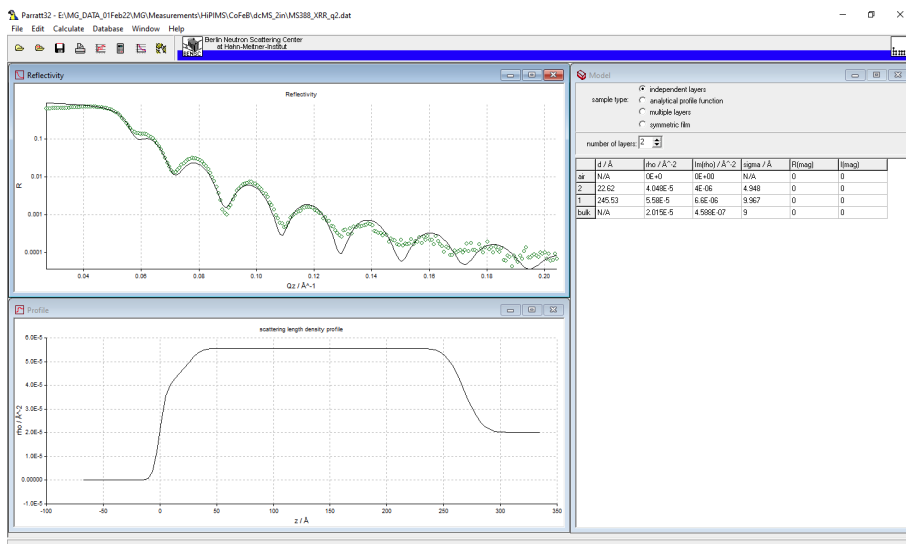


Fig. 1.23: XRR curve for thickness measurement of MgO/CoFeB sample, measured at UGC-CSR-DAE Indore.

1.11 Signal generator: R&S SMB100A



Fig. 1.24: Signal generator: R&S SMB100A

A signal generator is a device used to produce different signals at different frequencies. The R&S SMB100A signal generator can produce signals ranging from 0.01 Hz to 12.75 GHz. There are two output ports in the front panel; one port is for low-frequency signals ranging from 0.01 Hz to 1 MHz, and the other port is for radio frequency signals ranging from 100 kHz to 12.75 GHz. On the front panel, there is a screen and buttons to interact with the device.

1.12 Power supply: R&S NGL202



Fig. 1.25: Power Supply: R&S NGL202

A power supply is a two-quadrant device; it can act as a source, sink and constant resistance. It is usually used as a DC voltage source. It has two-independent channel that can be used to source or sink DC voltage.

1.13 Spectrum analyzer: R&S Spectrum rider FPH



Fig. 1.26: Spectrum analyzer: R&S Spectrum rider FPH

Spectrum analyzers are used for finding frequency response and real-time signal processing of radio frequency signals. The R&S Spectrum Rider FPH model 13 spectrum analyzer can work up to 13 GHz frequency. On the front panel, there is an LCD panel that displays the trace; it has buttons for putting marker(s) on traces, finding the center frequency, and adjusting the frequency range. It has inbuilt functionality to save previous settings. It also has a dedicated button for taking a snapshot of the trace.

1.14 Source Measuring Unit: Keithly 2450



Fig. 1.27: Source Measuring Unit (SMU): Keithly 2450

Source Measuring Unit (SMU) is a four-quadrant device; it can source and measure simultaneously. It is a very high precision device and has high

tolerance toward noise. It can also be used as a constant current source and used for resistance measurement.

1.15 Lock-in amplifier: SRS SR830

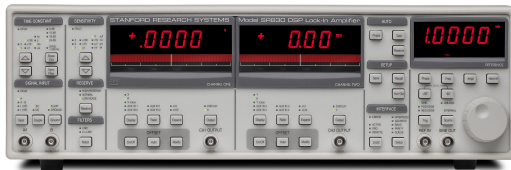


Fig. 1.28: Lock-in amplifier: SRS SR830

A lock-in amplifier is used to detect and measure a tiny AC signal. It is mostly used for rectifying signals buried with noise by locking the signal to a very small bandwidth. The Stanford research system SR830 lock-in amplifier can work from 0.01 Hz to 102 kHz. It has an internal oscillator, which can be used as the reference signal. It can take both single-ended input or differential input signals. On the front panel, three screens, out of which two show the X, R, and Y, θ values of the output signal, and the other screen shows the reference signal parameters.

1.16 Probe station

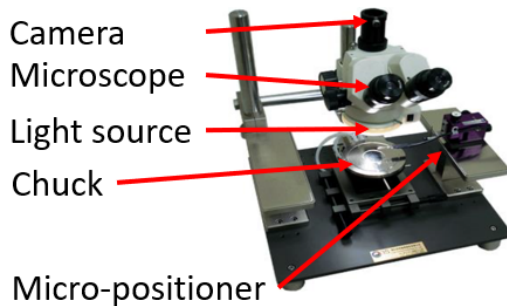


Fig. 1.29: Probe station

A probe station is used for the electrical measurement of samples with a smaller dimension which cannot be done with regular probes. The device consists of a chuck on top of which the samples are placed. There is a microscope and light source that enable visualization of the sample while making contacts. For making contacts, micropositioners are used, whose tips can be as small as $1 \mu\text{m}$ in diameter. The micropositioner can be connected to a power supply to apply the stimulus.

1.17 Oscilloscope

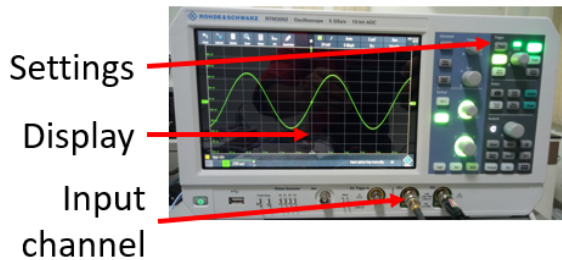


Fig. 1.30: Oscilloscope: R&S RTM3002

An oscilloscope is used for visualizing electrical signals and how they change over time. It is generally used to measure the AC voltage in circuits. It can do the Fourier analysis on any time-varying signal. The frequency range of the oscilloscope is 0.01 Hz to 100 MHz.

1.18 Other experimental apparatus

1.18.1 Spin coater

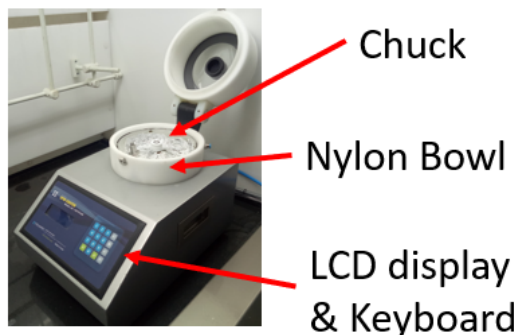


Fig. 1.31: Spin Coater: Holmarc HO-TH-05

For spin-coating PMMA of 100 nm thickness on a Si substrate, a Holmarc Spin-coater is used. It has a nylon bowl. Inside, a chuck holds the sample using a vacuum pump. There is an LCD and keyboard in the front panel to program the spin-coater's rotation speed, acceleration, period of rotation, and the number of steps.

1.18.2 Shaker

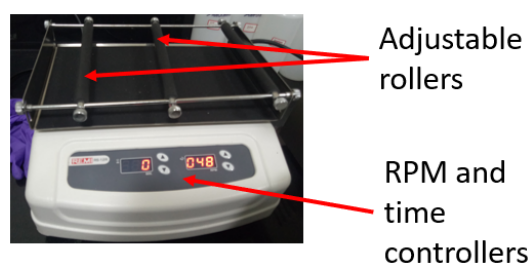


Fig. 1.32: Shaker: Remi RS-12R

To shake or to mix chemicals, the shaker is used. It has adjustable rollers, which help fix the beaker firmly on the movable platform. On the front panel, there are buttons to set the RPM and the time duration.

1.18.3 Hot plate

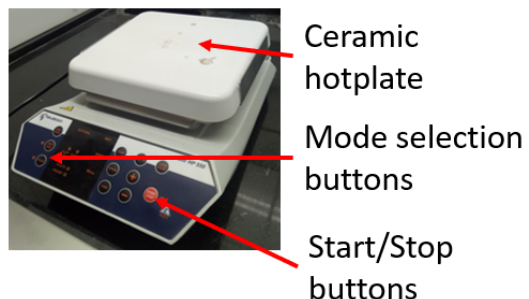


Fig. 1.33: Hot plate: Neuation iStir HP550

To bake samples at a high temperature, a hot plate is used. It has a ceramic platform over which samples are placed. The ceramic plate can go up to 550 °C . In the front panel, there are buttons to set the temperature, timer, and start/stop operations.

1.18.4 Ultrasonic cleaner



Fig. 1.34: Ultrasonic cleaner: Athena UAC

For cleaning samples, beakers, or other apparatus by vibrating at a high frequency to remove unwanted materials. Samples are placed inside a cleaner with an appropriate solvent that cleans while vibrating. There are buttons for start/stop, timer, and temperature in the front panel.

1.18.5 Hot air oven

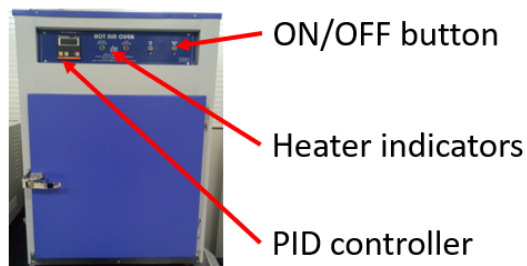


Fig. 1.35: Hot air oven

A hot air oven is used to sterilize the samples using dry air. Inside there is a thermostat to control the temperature. The inside wall is thermally insulated; hence it keeps the heat inside. On the front panel, it has an ON/OFF button, a heater indicator to indicate the heating status, and there is a PID controller, which controls the thermostat.

1.18.6 Rota mantle

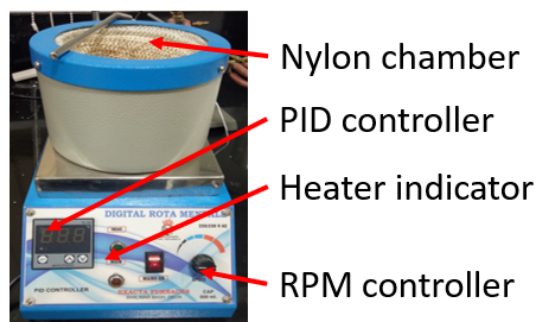


Fig. 1.36: Rota Mantle

For heating solvents while stirring with the help of a magnetic bead. They are usually used in the distillation process of chemicals. It has a nylon chamber inside which the glass apparatus, like a round-bottom flask, is placed. There is a PID controller on the front panel, which programs the heating. Then there is a heater indicator, which displays the heating status,

and there is an RPM controller, which controls the RPM of the magnetic bead used while stirring.

1.18.7 Nitrogen gun



Fig. 1.37: Nitrogen Gun

For cleaning of wafers by blowing N_2 gas. There is pipe all over the lab, which are connected to the N_2 cylinders, and there are outlets at work stations, where an air gun can be used to blow directly on the wafers.

1.18.8 Vacuum desiccator

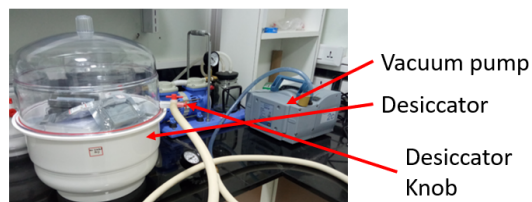


Fig. 1.38: Vacuum Desiccator

Samples that are prone to outside environment such as oxygen, moisture etc. are kept inside the vacuum desiccator. It is closed container after putting sample inside, the chamber is vacuum using a vacuum pump. After the desiccator is made vacuum, the knob to which the vacuum pump is connected is closed.

1.18.9 Muffle furnace

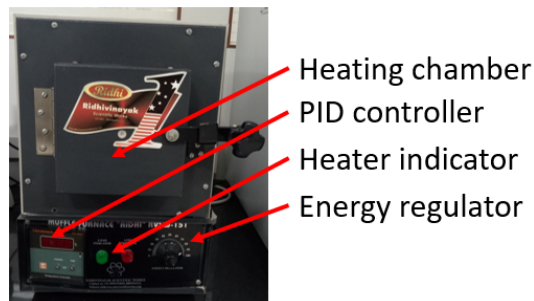


Fig. 1.39: Muffle furnace: Ridhi RVSW-151

To thermally anneal samples at a higher temperature to passivate all dangling bonds and structural imperfection. The muffle furnace can reach up to 1200 °C. In the front panel, there is a PID controller, which programs and regulates the furnace's heating. There is a heating indicator to indicate the heating status of the device. There is an energy regulator to control the power of the furnace. The samples are placed inside the heating chamber, which has insulated inner walls to prevent heat loss.

1.18.10 Fume hood



Fig. 1.40: Fume hood

Experiments which uses harmful chemicals or ejects harmful fumes is carried out inside the fume hood. It also prevents from accidental spillage of harmful chemicals, Inside there are nozzles for different gas like N_2 , O_2 , etc.

2. RESULTS

2.1 Character recognition system using neural network

2.1.1 Neural architecture modeling

For the character recognition system, initially, the model was given one hidden layer, and the number of hidden layer neurons was increased from 1 to 200. The respective error vs. no. of neurons was plotted. It is seen that after 40 neurons, the error gap started increasing. Therefore the first hidden layer has 40 hidden neurons. Now the model was given two hidden layers. The first hidden layer has 40 neurons, and the second hidden layer's neurons vary from 1 to 200. It is seen that the error gap started increasing after the 35th neuron. However, the error gap of the model with the two hidden layer systems was more than the single hidden layer system, which suggested that the model is overfitting. So to make sure, another hidden layer was added, and the same procedure was followed, the error gap increased even further. Hence the optimized number of hidden layers and hidden layer neurons is one hidden layer with 40 hidden neurons.

[35 input nodes] → [40 hidden nodes] → [26 output nodes]

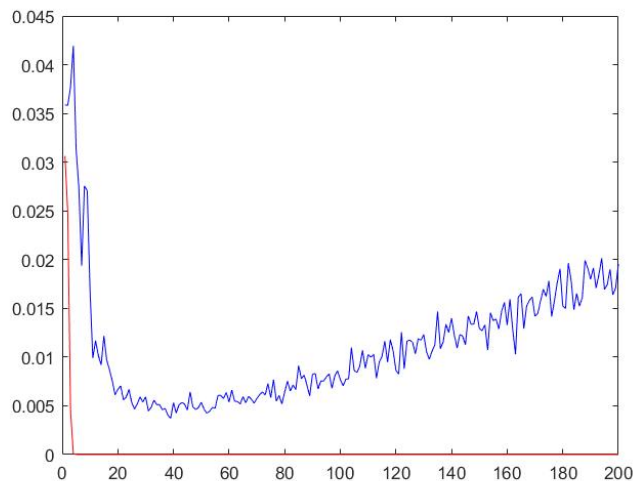


Fig. 2.1: Optimizing first hidden layer

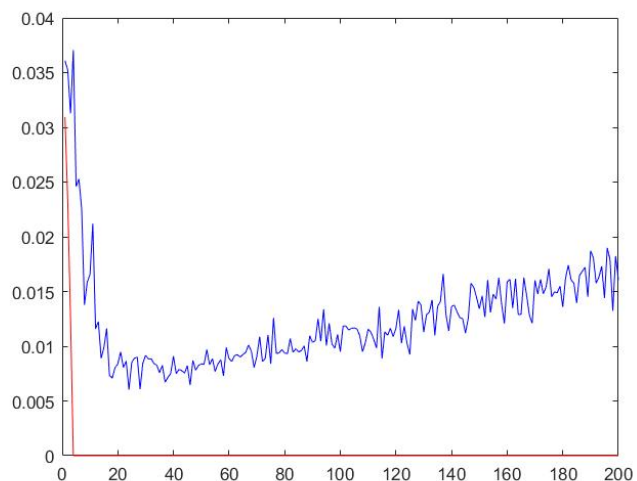


Fig. 2.2: Optimizing second hidden layer

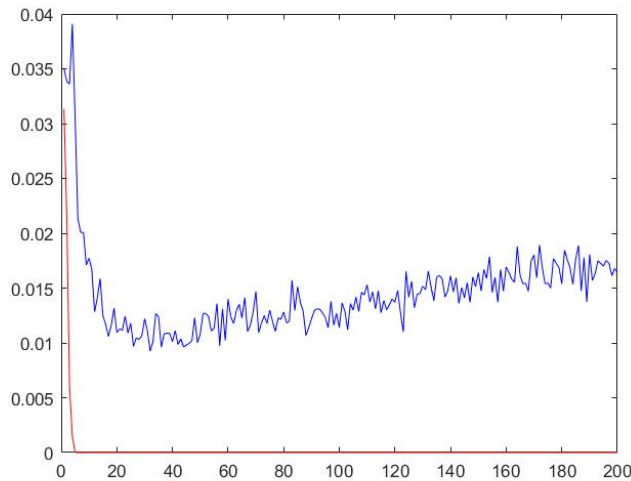


Fig. 2.3: Optimizing third hidden layer

2.1.2 Model output

The model was trained on 26 data depicting the original non-perturbed data, and the testing of the model was done on data with different degree of perturbation.

For 4-bit flip

Testing data: 520

No. of correct predictions: 424

No. of wrong predictions: 96

Accuracy of the model: 81.54%

For 6-bit flip

Testing data: 520

No. of correct predictions: 365

No. of wrong predictions: 155

Accuracy of the model: 70.19%

For (4 to 8)-bit flip

Testing data: 2678

No. of correct predictions: 1866

No. of wrong predictions: 812

Accuracy of the model: 69.68%

2.2 Improvement of magnetization using magnetic thermal annealing

To test the improvement of magnetization using magnetic thermal annealing. A magnetic sample was taken, from substrate side Ta(5)/MgO(0.8)/CoFeB(10) (All the numbers inside the bracket are the nominal thickness of the material deposited in nano-meter). This sample was processed through magnetic thermal annealing along the in-plane easy axis direction. The magnetic thermal annealing was done at 400 mT magnetic field, maintained at 400°C for 1 hour at 10^{-3} Torr in vacuum. The experimental VSM results of the sample before (in blue) and after (in red) the MTA is shown in the Figure 2.4.

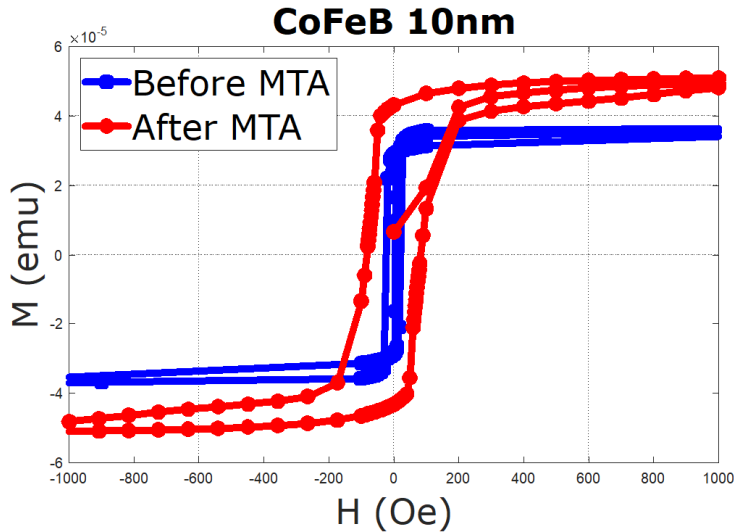


Fig. 2.4: VSM results of before and after MTA of MgO/CoFeB 10nm sample.

From the blue curve, it is seen that before MTA the CoFeB sample has a coercive field, $H_k = 21$ Oe and Magnetization, $M = 3.7 \times 10^{-5}$ emu. From the red curve, it is seen that after MTA, the CoFeB sample, has $H_k = 70$ Oe and $M=5.2 \times 10^{-5}$ emu. After MTA there is a 18.5 times more M-H area. Which suggest that upon doing magnetic thermal annealing, there is improvement in the magnetization of the CoFeB 10nm sample.

2.3 Development of LabView environment for different instruments

2.3.1 Power supply

To automate the power supply and for data acquisition, LabVIEW was used [1]. The two-channel power supply was automated to obtain the VI curve of a resistor and a diode and the input characteristics of a transistor.

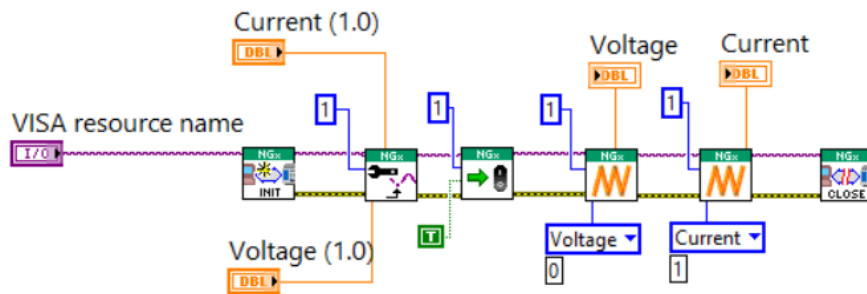


Fig. 2.5: LabVIEW automation of power supply R&S NGL202.

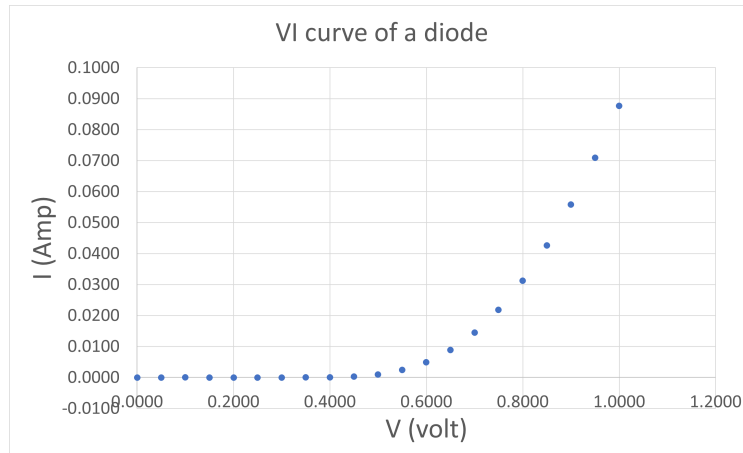


Fig. 2.6: VI automation of diode using power supply.

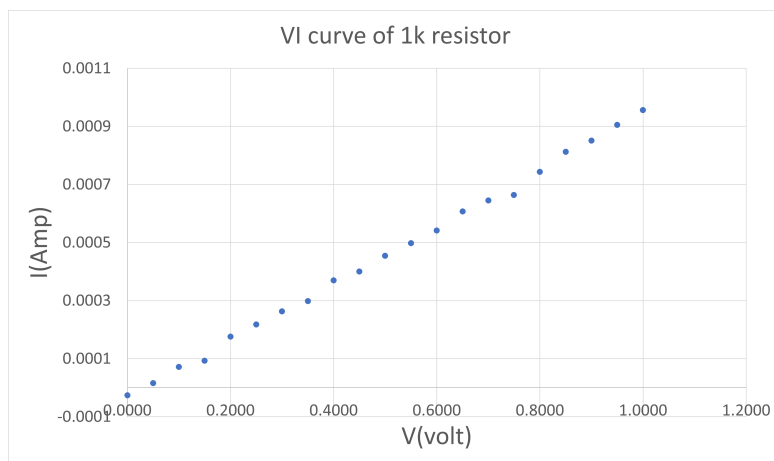


Fig. 2.7: VI automation of resistance using power supply.

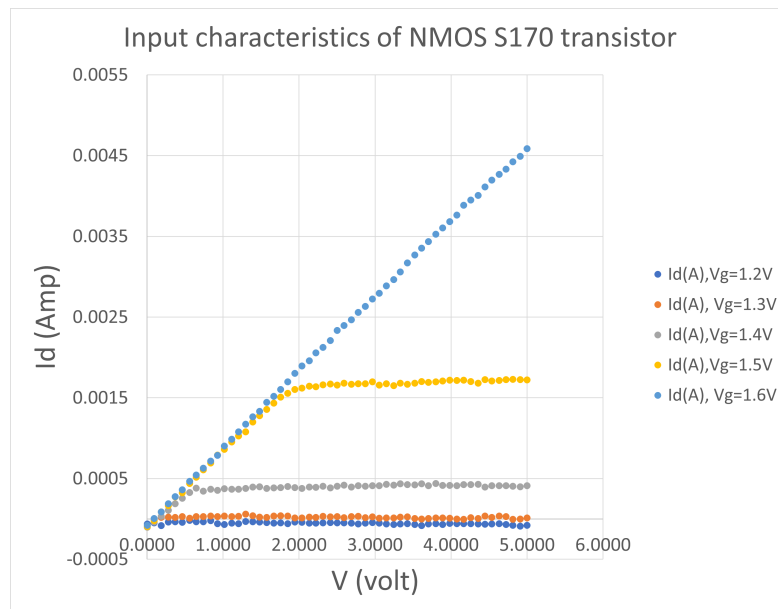


Fig. 2.8: VI automation of transistor using power supply.

2.3.2 Electromagnet

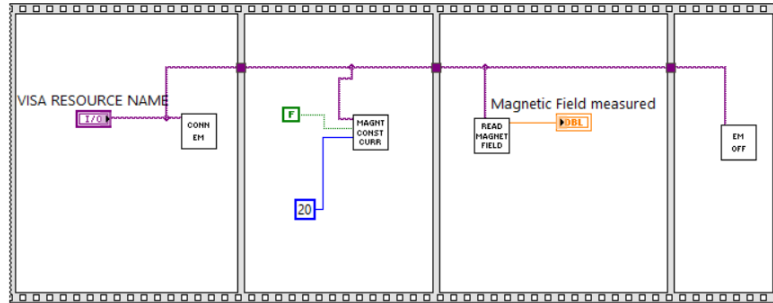


Fig. 2.9: LabVIEW: Electromagnet automation

The electromagnet was automated using LabVIEW. It was used to control the current flowing into the electromagnet's coil to change the constant magnetic field generated at the poles. It was also used to measure the magnetic field through a gauss probe connected to the controller of the electromagnet.

2.3.3 Signal generator

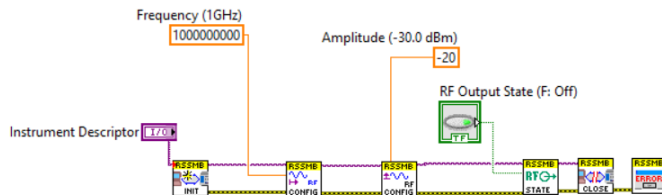


Fig. 2.10: LabVIEW: Signal generator automation

The signal generator was automated using LabVIEW. It was used to set different RF and LF frequencies of different amplitudes. With LabVIEW, the signal generator was automated to sweep from one frequency range to another frequency range.

2.3.4 Spectrum analyzer

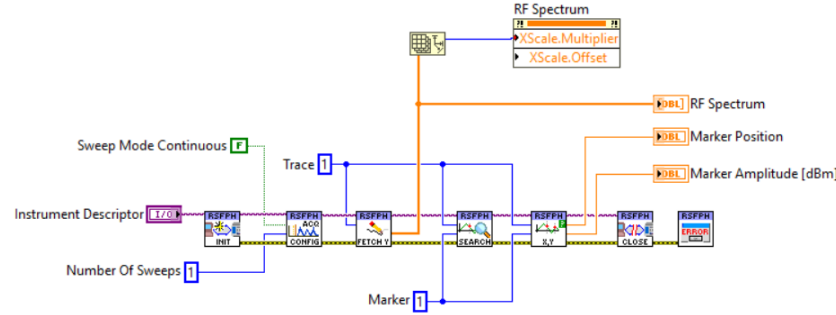


Fig. 2.11: LabVIEW: Spectrum analyzer automation

The spectrum analyzer was automated using LabVIEW to measure the power level of a given input signal, detects different frequency present in the signal. It was able to program the device, where to put the marker, setting the center frequency.

2.3.5 Lock-in amplifier

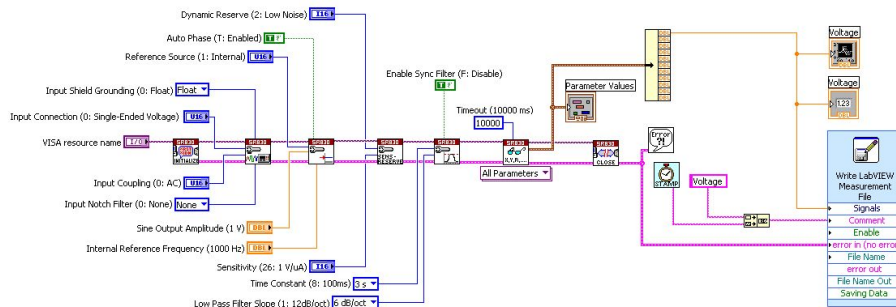


Fig. 2.12: LabVIEW: Lock-in amplifier automation

The Lock-in amplifier was automated using LabVIEW to remove noise from a signal by narrowing the bandwidth. It was automated to take single or differential mode input, setting up the sensitivity and the time constant. Apart from this, it can directly program the lock-in amplifier to set an internal reference frequency. The SR830 lock-in amplifier can detect the signal at 10kHz with bandwidth as narrow as 0.01 Hz.

2.4 Development of ferromagnetic resonance system

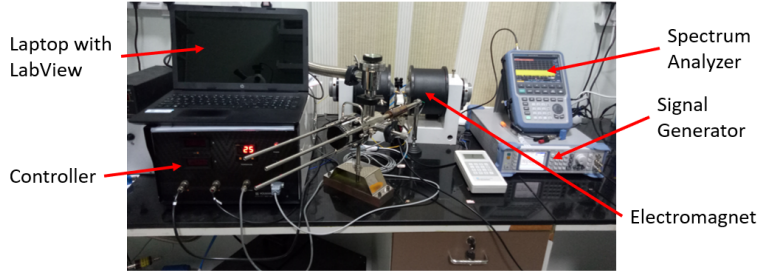


Fig. 2.13: Experimental system for ferromagnetic resonance.

The ferromagnetic resonance setup consists of an electromagnet, signal generator, spectrum analyzer, waveguide, and a laptop with LabVIEW. The magnetic sample is placed on top of the waveguide's signal channel. For in-plane ferromagnetic resonance, the longer side of the sample is placed in parallel to the signal line. The waveguide, along with the sample, is placed in between the poles of the electromagnet. The electromagnet generates the DC magnetic field, which causes the precession of the magnetization vector. To negative the damping of the magnetization vector, a transverse AC field is required, provided by the signal generator, connected to the input end of the waveguide. The output from the waveguide is fed into the spectrum analyzer to measure the FMR absorption.

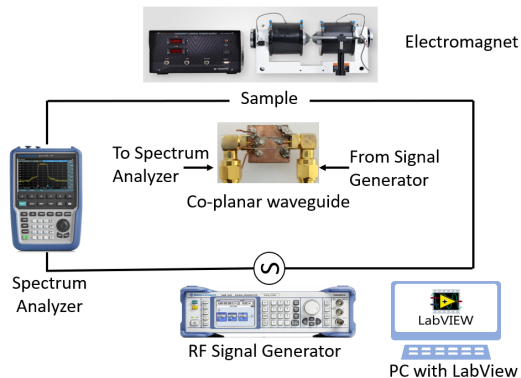


Fig. 2.14: Schematic of the ferromagnetic resonance system.

2.4.1 Characteristic impedance of coaxial cable

If the coaxial cable is terminated with a purely resistive load, R , the signal will be reflected or transmitted at the end of the line [8]. The transmission coefficient, T is given by:

$$T = \frac{2R}{R + Z_{cable}}$$

where

$$T = \frac{V_t}{V_0} = \frac{\text{transmitted signal}}{\text{incident signal}}$$

In a limiting case, if the resistive load is infinite, the transmission coefficient becomes 2, i.z. The transmitted pulse is twice the incident pulse,

$$\text{if } R \rightarrow \infty; T=2; V_t = 2V + 0$$

and if the resistive load is equal to the Z_{cable} , the transmission coefficient becomes 1, i.z. The transmitted pulse is same as the incident pulse.

$$\text{if } R \rightarrow Z_{cable}; T=1; V_t = 2V + 0$$

By adding a potentiometer in parallel, the transmitted signal can be measured as a function of R .

$$\frac{1}{T} = \frac{1}{2} + \frac{Z_{cable}}{2R}$$

The slope of this equation gives the Z_{cable} value.

V_0	V_t	R	T	$\frac{1}{2R}$	$\frac{1}{T}$
3.78	3.5623	100	0.9424	0.0050	1.0611
3.78	4.0866	200	1.0811	0.0025	0.9250
3.78	4.2679	300	1.1291	0.0017	0.8857
3.78	4.4100	400	1.1667	0.0013	0.8571
3.78	4.4900	500	1.1878	0.0010	0.8419
3.78	4.5810	600	1.2119	0.0008	0.8251
3.78	4.6550	700	1.2315	0.0007	0.8120
3.78	4.6840	800	1.2392	0.0006	0.8070
3.78	4.6990	900	1.2431	0.0006	0.8044
3.78	4.7530	1000	1.2574	0.0005	0.7953

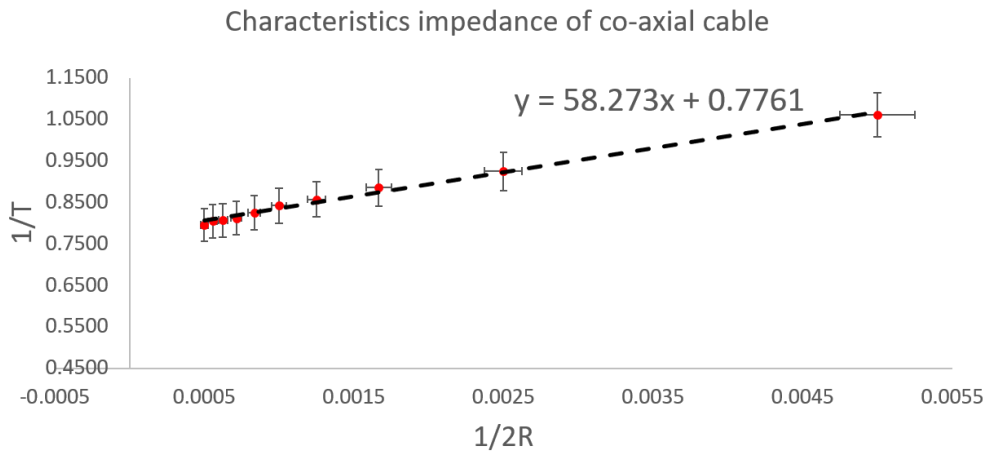


Fig. 2.15: Characteristics impedance of coaxial cable.

From the Figure 2.15, the fitted linear line gives the $Z_{cable} = 58.273\Omega$

2.4.2 Measurement of loss in the coaxial cable, connectors and the waveguide

The losses in the coaxial cable and connectors, are measured by the spectrum analyzer

Connection 1: Signal generator is connected to the spectrum analyzer

through an SMA cable (coaxial cable); from here, the loss due to a coaxial cable can be calculated.

Connection 2: Signal generator is connected to the waveguide using an SMA cable, and the output from the waveguide is connected to the spectrum analyzer through another SMA cable; from here, the loss due to the waveguide and 2x SMA cable can be calculated.

Connection 3: Same as Connection 2, with one L-connector connected to the waveguide; from here, the loss due to the waveguide, 2x SMA cable, and the L-connector can be calculated.

Connection 4: Same as Connection 3, with one additional T-connector connected to the other end of the waveguide; from here, the loss due to the waveguide, 2x SMA cable, the L-connector, and the T-connector can be calculated.

Connection 5: Same as Connection 3, with one additional $50\ \Omega$ termination to one open end of the T-connector; from here, the loss due to the waveguide, 2x SMA cable, the L-connector, the T-connector, and the $50\ \Omega$ termination can be calculated.

The signal generator was connected to the RF port at a frequency of 10 GHz and -10 dBm power.

Connections	Signal generator dbM	Spectrum analyzer dbM	loss (dBm)
Connection 1	-10	-25.5	15.5
Connection 2	-10	-43	33
Connection 3	-10	-49	39
Connection 4	-10	-44	34
Connection 5	-10	-49.4	39.4

Components	Loss(dBm)
SMA cables	15.5
Waveguide	2
L-connector	6
T-connector	-5
50 Ω termination	5.4

2.4.3 FMR result

This is the in-plane FMR output from the FMR setup of a hard disk, where the magnetic field was varied from 65 mT to 200 mT, and a 9 GHz RF signal was given to generate the transverse field.

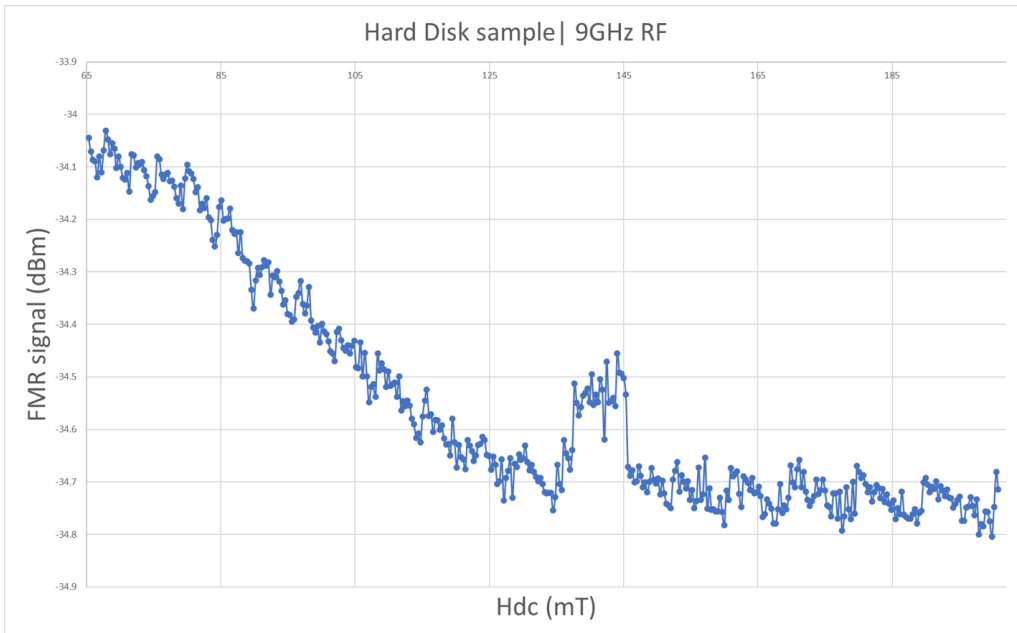


Fig. 2.16: FMR absorption of a magnetic hard disk sample.

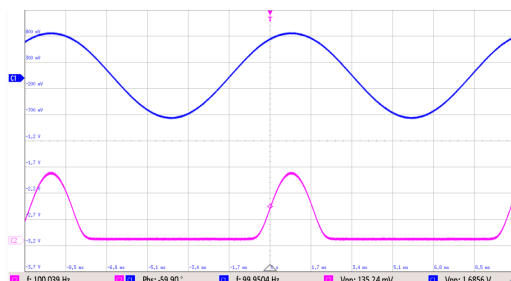
2.4.4 Schottky diode measurement results

The frequency of the output signal from the waveguide is in GHz, and the standard semi-conductor diode available can rectify AC signals up to 10 kHz frequency. Hence we use a Schottky diode to rectify the 9 GHz signal.

Schottky diodes are constructed using a metal electrode and N-type. Since the Schottky diode has a metal electrode on one side, it does not have the depletion region. The junction formed by the metal and the N-type material is the metal-semiconductor junction. The electron from the N-type material goes to the metal electrode in the forward bias. The drift of the majority of carriers enables the current to flow. In reverse bias, since there is no P-type material, there are no minority carriers to form the depletion region. The diode conduction stops very quickly, stopping the current flow, which is why it can operate at high RF frequencies.

Two Schottky diodes available in the market were tested, SRP BAT85 and Infineon diode BAT 6302. The following are the results tested on each diode at a different frequency and power level.

Schottky diode: SRP BAT85



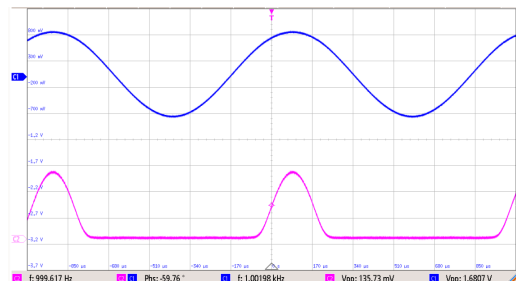
Input signal frequency: 100 Hz

Signal without rectifying

$$V_{pp} = 1.6856 \text{ V}$$

Signal after rectifying

$$V_{pp} = 135.24 \text{ mV}$$



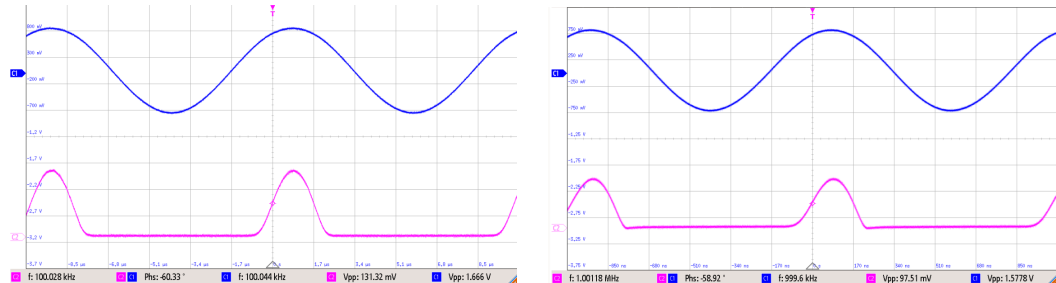
Input signal frequency: 1 kHz

Signal without rectifying

$$V_{pp} = 1.6807 \text{ V}$$

Signal after rectifying

$$V_{pp} = 135.73 \text{ mV}$$



Input signal frequency: 100 kHz

Signal without rectifying

$$V_{pp} = 1.666 \text{ V}$$

Signal after rectifying

$$V_{pp} = 131.32 \text{ mV}$$

Input signal frequency: 1 MHz

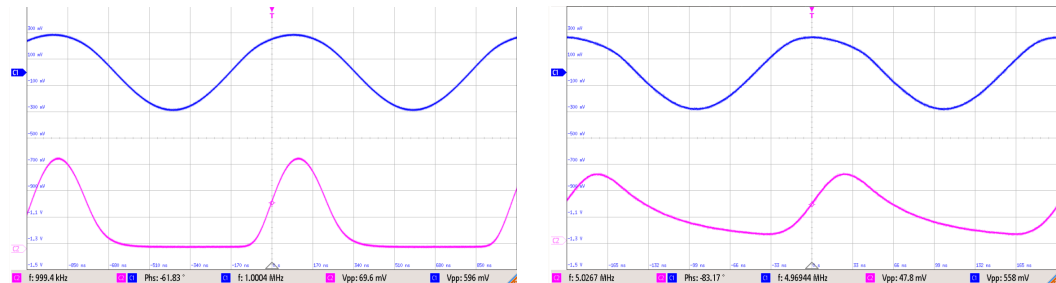
Signal without rectifying

$$V_{pp} = 1.5778 \text{ V}$$

Signal after rectifying

$$V_{pp} = 97.51 \text{ mV}$$

Schottky diode: Infineon BAT6302



Input signal frequency: 1 MHz

Signal without rectifying

$$V_{pp} = 596 \text{ mV}$$

Signal after rectifying

$$V_{pp} = 69.6 \text{ mV}$$

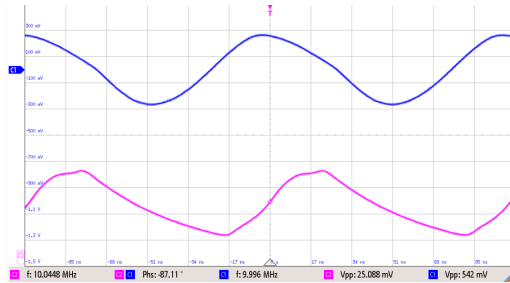
Input signal frequency: 5 MHz

Signal without rectifying

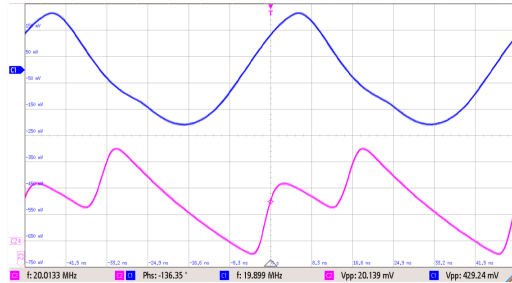
$$V_{pp} = 558 \text{ mV}$$

Signal after rectifying

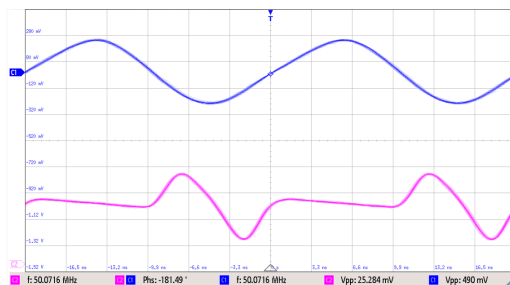
$$V_{pp} = 47.8 \text{ mV}$$



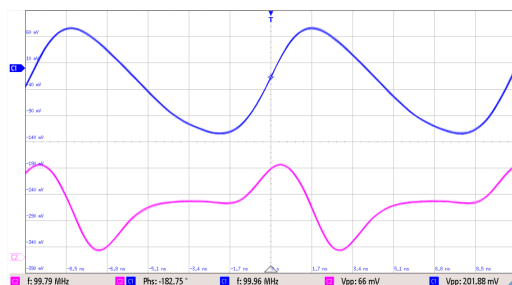
Input signal frequency: 10 MHz
Signal without rectifying
 $V_{pp} = 542 \text{ mV}$
Signal after rectifying
 $V_{pp} = 25.088 \text{ mV}$



Input signal frequency: 20 MHz
Signal without rectifying
 $V_{pp} = 429.24 \text{ mV}$
Signal after rectifying
 $V_{pp} = 20.139 \text{ mV}$

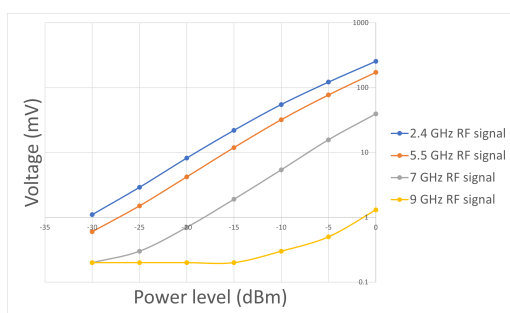


Input signal frequency: 50 MHz
Signal without rectifying
 $V_{pp} = 490 \text{ mV}$
Signal after rectifying
 $V_{pp} = 25.284 \text{ mV}$



Input signal frequency: 100 MHz
Signal without rectifying
 $V_{pp} = 201.88 \text{ mV}$
Signal after rectifying
 $V_{pp} = 66 \text{ mV}$

The infenion BAT6302 schottky diode DC voltage was measured for different power level of the RF signal at different frequency.



2.5 Electron beam lithography patterns

After calibrating the parameters of the thin-film deposition of PMN-PT, FeGa, we need to see the domain formation and other properties of the PMN-PT and FeGa in nanostructures. The aim is to produce single-domain nanomagnets of different thicknesses.

The deposition will be done on a silicon substrate of 3×1.5 mm. There will be $30, 100 \times 100 \mu\text{m}$ boxes, inside which there will be nanostructures of different shapes and sizes.

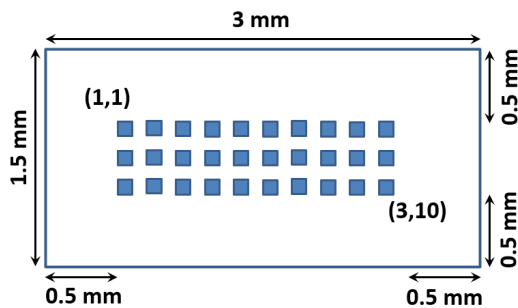


Fig. 2.17: EBL patterns on $3 \text{ mm} \times 1.5 \text{ mm}$ Si substrate.

For **FeGa**, in total, there will be three different thicknesses in between 1 to 2 nm

For each thickness, there are elliptical and circular structures. The reason behind elliptical structures is to stabilize the nanomagnets in case of in-plane magnetic anisotropy, and the circular structures will stabilize in case of perpendicular anisotropy.

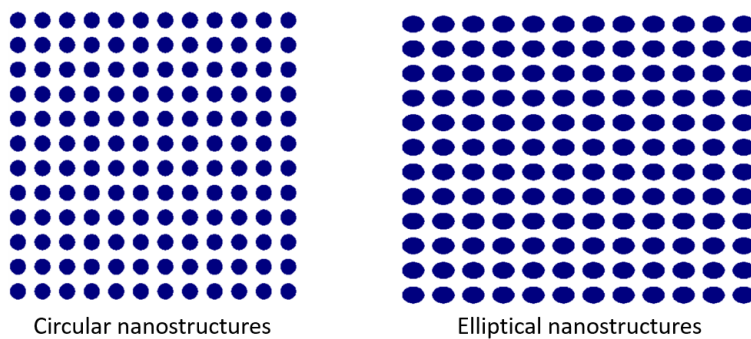


Fig. 2.18: Circular and elliptical EBL patterns.

Here, FeGa with 1 nm thickness structures is expected to reflect perpendicular magnetic anisotropy and 2 nm thickness, which will reflect in-plane magnetic anisotropy. However, for each thickness, both structures are included because it is not sure at what thickness anisotropy comes into play, so for a comparative study, both the structures are included. Except for nanostructures, there is also a large circular structure of 100 um diameter to form a multidomain magnet. The structure shape and sizes are

Elliptical (all numbers are in nm)

$250 \times 200, 200 \times 150, 150 \times 100, 110 \times 50$

Circular (all numbers are in nm)(diameter)

50, 75, 100, 125, 150

2.6 Sputtering deposition

Before fabricating the device, it is needed to calibrate the parameters of the magnetostrictive and piezoelectric material, such as damping parameter α , dielectric coefficient and so on. Kapton can be used as a substrate for the thin film since it is flexible and can endure high temperatures. PMN-PT is used for piezoelectric and for magnetostrictive material, FeGa.

All deposition is from the substrate side, and all the numbers inside the bracket are the nominal thickness in nm.

Thin-film 1

Kapton/PMN-PT (25, 50, 75, 100)

From this thin film, for different thicknesses of PMN-PT, the d_{33} , Young's modulus, and Poisson ratio can be calculated.

Thin-film 2

Kapton/PMN-PT (25, 50, 75, 100)/FeGa(0.8, 1, 1.5, 1.7, 2, 5, 10, 20, 50, 100)

From this thin film, for different thicknesses of PMN-PT and FeGa, the damping parameter α can be calibrated by obtaining the MH hysteresis, the

saturation magnetization, and the coercive field is calculated.

Thin-film 3

Kapton/PMN-PT(50)/FeGa(2)/ Al_2O_3 (40)/CoFeB(2)MgO(0.8)/CoFeB(2)/Ta(5)/Ru(5)/Cr or Au

This thin film suggests the entire stack, which can be used as one single neuron. Here we have the multiferroic, and on top of that, we have the read/write measuring unit.

Thin-film 4

Kapton/PMN-PT(50)/FeGa(2)/MgO(0.8)/CoFeB(2)/Ta(5)/Ru(5)/Cr or Au

This thin film is a modification of the thin-film 3, and here it is tried to get the TMR property in between FeGa and CoFeB using a MgO spacer, thereby reducing the stack into a compact version.

Thin-film 5

Kapton/PMN-PT(50)/FeGa(2)/MgO(0.8)/CoFeB(2)

This thin film is the same as Thin-film 4, except for the outer metallic contact layer to visualize the magnetization of the top CoFeB layer by MFM.

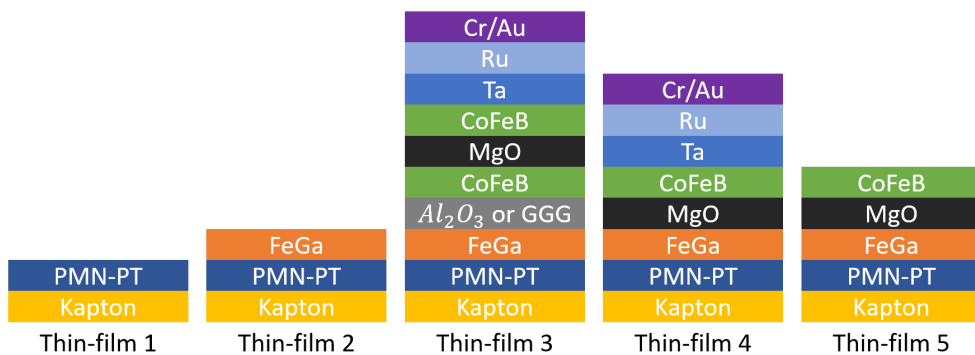


Fig. 2.19: Sputtering deposition of thin-films.

2.7 Neuromorphic devices using multiferroics

We plan to use multiferroics and tunnelling junction for neuromorphic device architecture. The multiferroics part will deal with summation of input and activation function, and the tunnelling junction will deal with weight and the output of the neuron.

2.7.1 Device architecture

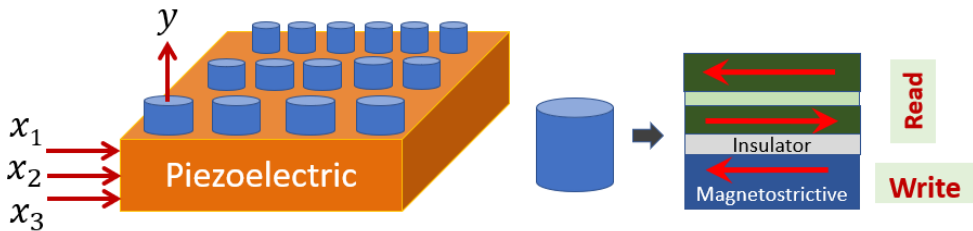


Fig. 2.20: Hardware architecture of a single neuron.

A single neuron of the device consists of the piezoelectric layer, on top of which there are many pillars. These pillars are made up of magnetostrictive material, and on top of the magnetostrictive material, there is a tri-layer exhibiting the TMR. The pillars are of different areas. The inputs are fed at the piezoelectric layer, and this generates the strain, which is transferred to the magnetostrictive nanomagnets present in the pillars. The stress anisotropy in the magnetostrictive material affects the energy barrier of the tri-layer magnet, causing parallel and anti-parallel orientation. In this architecture, the piezoelectric material serves the purpose of summation block, as if two voltage inputs are given, it will generate strain based on the two inputs [28]. The tri-layer serves the purpose of the weight of edges. Therefore as many neurons are connected to this neuron, that many numbers of pillars will be there on the piezoelectric material [34].

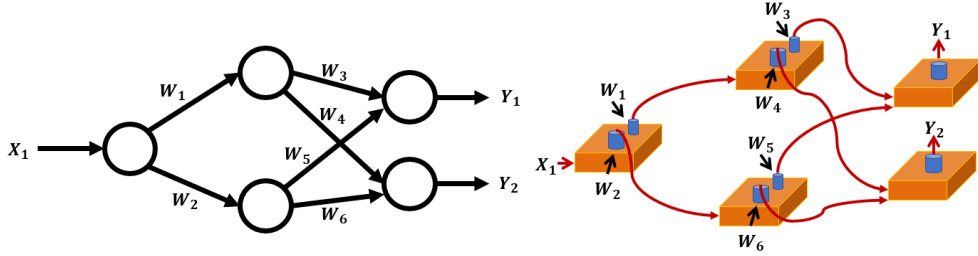


Fig. 2.21: Neuromorphic hardware architecture of a full neural network.

In the Figure 2.21, the neural network hardware architecture is compared with an abstract neural network. The abstract network has one neuron in the input layer, two hidden neurons in the hidden layer, and two in the output layer. All the edges connecting to the neurons have weight $W_1, W_2, W_3, W_4, W_5, W_6$. X_1 is the input given to the network, and Y_1 and Y_2 are the network's output. The weight are encoded inside the read/write unit or the blue pillars.

2.7.2 Multiferroics

For a thin-film deposition, we have chosen lead magnesium niobate-lead titanate (PMN-PT) as piezoelectric material and iron-gallium (FeGa) as magnetostrictive material [18]. FeGa is deposited on PMN-PT. A voltage of 50 mV is applied across the deposition. It creates strain on the piezoelectric material [2, 29].

$$\epsilon_{piezo} = d_{piezo} \times \frac{V_{in}}{t_{piezo}}$$

where $d_{piezo}=3000$ pm/V for PMN-PT, $t_{piezo}=100$ nm [32]. The strain is elastically transferred to the magnetostrictive material.

$$\epsilon_{mag} = \epsilon_{piezo}$$

This creates stress anisotropy in the FeGa layer, stress, $\sigma = Y\epsilon_{mag}$, Young's modulus of FeGa, $Y=250 \times 10^9$ Pa, and $\frac{3}{2}\lambda = 150 \times 10^{-6}$

$$\text{Stress anisotropy (FeGa)} = \frac{3}{2}\lambda\sigma\Omega\cos^2\theta = 2.4 \times 10^{-18} J$$

2.7.3 Read unit using tunnel junctions

The stress anisotropy generated from the PMN-PT/FeGa multilayer should be able to reduce the energy barrier of the tri-magnetic layer exhibiting the TMR, for magnetization switching. As a result, parallel and anti-parallel orientation in the tri-layer is possible [16].

The resistance area product of the parallel orientation of a TMR,

$$R_P A = 175 \text{ } k\Omega\mu\text{m}^2$$

R_P is the resistance of TMR when both the magnets are in the parallel direction, and the desired TMR value is 300% [26].

$$TMR = \frac{R_{AP}}{R_P} - 1$$

Hence $R_{AP} = 4R_P$

$$R_{AP} A = 700 \text{ } k\Omega\mu\text{m}^2$$

If a constant current, $I_{read} = 1 \text{ nA}$ is given to the TMR of area $100 \text{ nm} \times 100 \text{ nm}$

$$V_P = I_{read} \cdot \frac{R_P A}{A} = 17.5 \text{ mV}$$

$$V_{AP} = I_{read} \cdot \frac{R_{AP} A}{A} = 70 \text{ mV}$$

That is to make the TMR in parallel orientation, 17.5 mV is required and to make anti-parallel orientation, 70 mV is required.

We can encapsulate, $V_P = 17.5 \text{ mV}$ as weight, $W = 0$ and $V_P = 70.0 \text{ mV}$ as $W = 1$. It does not necessarily have to be parallel or anti-parallel orientation, i.e. the angle between the free and the fixed layer magnetization, θ_f should not always be 0° or 180° . It can also be 0° and 90° , or 180° and 90° .

$$G(\theta_f) = G_{90^\circ}(1 - \eta \cos \theta_f)$$

where G denotes the conductance and

$$\eta = \frac{G_P - G_{AP}}{G_P + G_{AP}}$$

$G_{AP} = G(180^0)$ and $G_P = G(0^0)$

$$TMR = \frac{G_P - G_{AP}}{G_{AP}}$$

Hence, η can be expressed as

$$\eta = \frac{TMR}{TMR + 2}$$

if $\theta_f = 0^0$ or 180^0 , $G(\theta_f) = G_{90^0}(1 - \eta)$

and if $\theta_f = 90^0$, $G(\theta_f) = G_{90^0}$

We can encapsulate,

$\theta_f = 90^0$ as W=0, and

$\theta_f = 0^0$ or 180^0 as W=1.

3. DISCUSSIONS AND CONCLUSIONS

From the results of the character recognition model it is seen that increasing the number of neurons in the hidden layer or the hidden layer itself will not give good accuracy. And from the predicted results of the model it is seen that adding more noises to the data causes malfunction of the model and gives bad accuracy.

From the magnetic thermal annealing of the MgO(0.8)/CoFeB(10) (the numbers are in nm) sample, it is seen that the M-H area after MTA is 18.5 times more than before MTA. This reflects that the structural imperfection of the MgO/CoFeB sample, which was deteriorating the overall magnetization, is removed—giving rise to higher magnetization in the easy axis of the sample.

To achieve massive parallel processing like in the human brain, mimicking the brain's neural architecture is the ultimate solution for neuromorphic computing. Choosing PMN-PT and FeGa for the multiferroic composite layer makes the device energy-efficient. Moreover, the perpendicular anisotropy of the magnetic layers can reduce the lateral dimension to accommodate more number of nanopillars in a given of area.

The design of the neuromorphic hardware are based on realistic parameters and are feasible to do produce this device which would provide low energy neuromorphic computing.

3.1 Future plans

The thickness dependence of material parameters for piezoelectric and magnetostrictive layers need to be calibrated. The perpendicular anisotropy formed between the interface of the two magnetic layers requires calibration. Calibration of the PMN-PT/FeGa interface is required. We need to check the read/write unit formation between CoFeB/MgO/FeGa.

Once all the calibration of the thin-film sample is done. EBL sputtering will be carried out based on the EBL patterns from where deposition and characterization of nanomagnets will be done. The nanomagnets need to be characterized for domain formation, magnetic anisotropy, and dipole coupling effect. The area dependence of read/write unit for weights needs to be calibrated and based on the calibration data, the EBL patterning needs to be done. After calibration and characterization, the final deposition of the neuron will be done, which will be connected to other neurons using multi-levels of lithography.

BIBLIOGRAPHY

- [1] Labview. <https://www.ni.com/en-in/shop/services /products/labview-core-1-course.html>, January 2020.
- [2] S. R. Anton and H. A. Sodano. A review of power harvesting using piezoelectric materials (2003-2006). *Smart Mater. Struct.*, 16:R1, 2007.
- [3] Mario Norberto Baibich, Jean Marc Broto, Albert Fert, F Nguyen Van Dau, Frédéric Petroff, P Etienne, G Creuzet, A Friederich, and J Chazelas. Giant magnetoresistance of (001) fe/(001) cr magnetic superlattices. *Physical Review Letters*, 61(21):2472, 1988.
- [4] Grünberg Binasch, Peter Grünberg, F Saurenbach, and W Zinn. Enhanced magnetoresistance in layered magnetic structures with antiferromagnetic interlayer exchange. *Physical review B*, 39(7):4828, 1989.
- [5] T. Brintlinger, S. H. Lim, K. H. Baloch, P. Alexander, Y. Qi, J. Barry, J. Melngailis, L. Salamanca-Riba, I. Takeuchi, and J. Cumings. In situ observation of reversible nanomagnetic switching induced by electric fields. *Nano Lett.*, 10(4):1219–1223, 2010.
- [6] S. Chikazumi. *Physics of Ferromagnetism*. Oxford University Press, USA, 1997.
- [7] W. Eerenstein, N. D. Mathur, and J. F. Scott. Multiferroic and magnetoelectric materials. *Nature*, 442(7104):759–765, 2006.
- [8] P Fonseca, ACF Santos, and EC Montenegro. A very simple way to measure coaxial cable impedance. *Revista Brasileira de Ensino de Física*, 29:373–375, 2007.

- [9] W. J. Gallagher and S. S. P. Parkin. Development of the magnetic tunnel junction MRAM at IBM: from first junctions to a 16-Mb MRAM demonstrator chip. *IBM J. Res. Dev.*, 50(1):5–23, 2006.
- [10] T. L. Gilbert. A phenomenological theory of damping in ferromagnetic materials. *IEEE Trans. Magn.*, 40(6):3443, 2004.
- [11] Geoffrey Hinton, Yann LeCun, and Yoshua Bengio. Deep learning. *Nature*, 521(7553):436–444, 2015.
- [12] John J Hopfield. Neural networks and physical systems with emergent collective computational abilities. *Proceedings of the national academy of sciences*, 79(8):2554–2558, 1982.
- [13] S Ikeda, K Miura, H Yamamoto, K Mizunuma, HD Gan, M Endo, SI Kanai, J Hayakawa, F Matsukura, and H Ohno. A perpendicular-anisotropy cofeb–mgo magnetic tunnel junction. *Nature materials*, 9(9):721–724, 2010.
- [14] Michel Julliere. Tunneling between ferromagnetic films. *Physics letters A*, 54(3):225–226, 1975.
- [15] R. Kellogg and A. Flatau. Experimental investigation of Terfenol-D’s elastic modulus. *J. Intell. Mater. Sys. Struc.*, 19(5):583–595, 2007.
- [16] J. S. Kilby. *Turning potential into realities: the invention of the integrated circuit*. Nobel Lecture in Physics, The Nobel Foundation, Sweden, 2000.
- [17] L. Landau and E. Lifshitz. On the theory of the dispersion of magnetic permeability in ferromagnetic bodies. *Phys. Z. Sowjet.*, 8:153, 1935.
- [18] M. Liu, S. Li, Z. Zhou, S. Beguhn, J. Lou, F. Xu, T. J. Lu, and N. X. Sun. Electrically induced enormous magnetic anisotropy in Terfenol-D/lead zinc niobate-lead titanate multiferroic heterostructures. *J. Appl. Phys.*, 112(6):063917, 2012.

- [19] Carver Mead. Adaptive retina. In *Analog VLSI implementation of neural systems*, pages 239–246. Springer, 1989.
- [20] S Miwa, S Ishibashi, H Tomita, T Nozaki, E Tamura, K Ando, N Mizuochi, T Saruya, H Kubota, K Yakushiji, et al. Highly sensitive nanoscale spin-torque diode. *Nature materials*, 13(1):50–56, 2014.
- [21] Jagadeesh Subbaiah Moodera, Lisa R Kinder, Terrilyn M Wong, and R Meservey. Large magnetoresistance at room temperature in ferromagnetic thin film tunnel junctions. *Physical review letters*, 74(16):3273, 1995.
- [22] O. Mosendz, J. E. Pearson, F. Y. Fradin, G. E. W. Bauer, S. D. Bader, and A. Hoffmann. Quantifying spin Hall angles from spin pumping: Experiments and theory. *Phys. Rev. Lett.*, 104(4):046601, 2010.
- [23] O. Mosendz, V. Vlaminck, J. E. Pearson, F. Y. Fradin, G. E. W. Bauer, S. D. Bader, and A. Hoffmann. Detection and quantification of inverse spin Hall effect from spin pumping in permalloy/normal metal bilayers. *Phys. Rev. B*, 82(21):214403, 2010.
- [24] C. W. Nan, M. I. Bichurin, S. Dong, D. Viehland, and G. Srinivasan. Multiferroic magnetoelectric composites: Historical perspective, status, and future directions. *J. Appl. Phys.*, 103(3):031101, 2008.
- [25] News. Switching up spin. *Nature*, 476(7375), Aug. 25, 2011. doi:10.1038/476375c.
- [26] S. S. P. Parkin, C. Kaiser, A. Panchula, P. M. Rice, B. Hughes, M. G. Samant, and S. H. Yang. Giant tunnelling magnetoresistance at room temperature with MgO (100) tunnel barriers. *Nature Mater.*, 3(12):862–867, 2004.
- [27] Chi-Sang Poon and Kuan Zhou. Neuromorphic silicon neurons and large-scale neural networks: challenges and opportunities. *Frontiers in neuroscience*, 5:108, 2011.

- [28] K. Roy. Ultra-low-energy non-volatile straintronic computing using single multiferroic composites. *Appl. Phys. Lett.*, 103(17):173110, 2013.
- [29] K. Roy. Dynamical systems study in single-phase multiferroic materials. *Europhys. Lett.*, 108(6):67002, 2014.
- [30] K. Roy. Electric field-induced magnetization switching in interface-coupled multiferroic heterostructures: a highly-dense, non-volatile, and ultra-low-energy computing paradigm. *J. Phys. D: Appl. Phys.*, 47(25):252002, 2014.
- [31] K. Roy. Landauer limit of energy dissipation in a magnetostrictive particle. *J. Phys.: Condens. Matter*, 26(49):492203, 2014.
- [32] K. Roy. Ultra-low-energy straintronics using multiferroic composites. In *Proc. SPIE Nanoscience (Spintronics VII) 9167, 91670U*, 2014.
- [33] K. Roy. Area-delay-energy trade-offs of strain-mediated multiferroic devices. *IEEE Trans. Magn.*, 51(6):2500808, 2015.
- [34] K. Roy. Separating read and write units in multiferroic devices. *Sci. Rep.*, 5:10822, 2015.
- [35] Kuntal Roy. Spintronics: recent developments on ultra-low-energy, area-efficient, and fast spin-devices and spin-circuits. In *TechConnect Briefs (NanoTech) 2017*, volume 5, pages 51–54, 2017.
- [36] Kuntal Roy. Ultralow energy analog straintronics using multiferroic composites. *IEEE Transactions on Nanotechnology*, 16(2):333–346, 2017.
- [37] Kuntal Roy. Energy-efficient multiferroic spin-devices and spin-circuits. In *Spin*, volume 10, page 2030001. World Scientific, 2020.
- [38] G. Srinivasan. Magnetoelectric composites. *Annu. Rev. Mater. Res.*, 40:153–178, 2010.
- [39] John Yon Neumann. The computer and the brain. *New Haven, Conn.: Yale Uni*, 1958.

- [40] H. Zhao, A. Lyle, Y. Zhang, P. K. Amiri, G. Rowlands, Z. Zeng, J. Kagine, H. Jiang, K. Galatsis, K. L. Wang, I. N. Krivorotov, and J. P. Wang. Low writing energy and sub nanosecond spin torque transfer switching of in-plane magnetic tunnel junction for spin torque transfer random access memory. *J. Appl. Phys.*, 109(7):07C720, 2011.